UNIVERSITÉ DU QUÉBEC À MONTRÉAL

# UTILISATION DE L'EXCÈS DE $^{230}$Th POUR DÉTERMINER LES TAUX DE SÉDIMENTATION ET LES EFFETS DIAGÉNÉTIQUES DANS DES SÉDIMENTS DU SUD DE LA RIDE DE LOMONOSOV

MÉMOIRE

PRÉSENTÉ
COMME EXIGENCE PARTIELLE
DE LA MAÎTRISE EN SCIENCES DE LA TERRE

PAR
KARL PURCELL

Avril 2020

# ACKNOWLEDGEMENTS

I want to first thank Claude Hillaire-Marcel and Anne De Vernal to have believed in me, that I was up to the task, and also to have made it possible for me to go on an incredible adventure aboard the CCGS Amundsen. Special thanks to Bassam Ghaleb who, even though he works very very long hours, took the time to teach me how to use many techniques and lab instruments, and answer any questions I had, or endure the mistakes I made. Thanks to everyone who helped this project move forward with samples, analyses, or lab training (Agnieszka Adamowicz, André Poirier, François Hardy, Jean-François Hélie, Julien Gogot, Michel Preda, Pierre-Marc Godbout, Rüdiger Stein, and the PS27 expedition scientists). Thanks to the geophysicists for their free champagne, beer, liquor, and friendship. Thanks to my office neighbors for all the good times, and Charles-Élie Dubé-Poirier for his extraordinary mapmaking skills. Thanks to everyone in the micropaleontology lab for their help, especially Cynthia Leduc. Big thanks to my family for their love, support, and proofreading abilities!

# FOREWORD

The research presented in this master thesis examines two sediment cores; PS2757-6 and PS2757-8 taken from nearby sites during the Arctic Expedition ARK-XI/1 (or PS27) of RV "Polarstern" in 1995. This expedition is described in the scientific cruise report (Rachor, 1997). U-Series analysis were done at Geotop-UQAM under the supervision of Bassam Ghaleb and André Poirier. Carbon and nitrogen percentage, and $\delta^{13}C$ analyses were done at Geotop-UQAM by Agnieszka Adamowicz and Jean-François Hélie. In addition to U-series and stable isotopes measurements, we included some grain size, mineralogical, geochemical and micropaleontological results from previous studies on core PS2757-8. Grain size and mineralogy measurements are from Müller and Stein, (2000). Wet bulk density was taken in Niessen (1996). Geochemistry was taken from Schoster (2005). Micropaleontological analysis were done by Matthiessen et al. (2001).

# TABLE OF CONTENTS

# LIST OF FIGURES

# LIST OF ABBREVIATIONS AND ACRONYMS

| | |
|---|---|
| AR | Activity Ratio |
| BP | Before Present |
| C | Carbon |
| $C_{inorg}$ | Total inorganic carbon |
| $C_{org}$ | Total organic carbon |
| $C_{tot}$ | Total carbon |
| cal. yr | Calibrated year |
| cf. | *Confer* (Compare) |
| COC | Colloïdal organic carbon |
| DOC | Dissolved organic carbon |
| e.g. | *Exempli gratia* (for exemple) |
| et al. | *Et alli* (and others) |
| HCL | Hydrochloric acid |
| HF | Hydrofluoric acid |
| $HNO_3$ | Nitric acid |
| $H_3BO_3$ | Boric acid |
| i.e. | *id est* (that is) |
| IRD | Ice-rafted debris |
| KAL | Kastenlot corer |
| LGM | Last Glacial Maximum |
| MC-ICPMS | Multicollector-Inductively Coupled Plasma Mass Spectrometer |
| MIS | Marine isotopic stage |

| | |
|---|---|
| MUC | Multicorer |
| N | Nitrogen |
| NM | Nautical miles (1852 metres) |
| Ntot | Total nitrogen |
| Pa | Protactinium |
| Pb | Lead |
| PS27 | 27th expedition of RV "Polarstern", or ARK-IX/4 |
| pmol/g | $10^{-12}$ moles per gram |
| Ra | Radium |
| RV | Research vessel |
| SPM | Suspended particulate matter |
| Th | Thorium |
| TPD | Transpolar Drift |
| XRD | X-ray diffraction |

# LIST OF SYMBOLS AND UNITS

| | |
|---|---|
| % | Percent |
| ‰ | Per mil |
| < | Smaller than |
| > | Bigger than |
| ~ | Approximately |
| ± | Plus or minus |
| δ | Delta |
| Φ | Phi |
| σ | Sigma |
| °C | Degrees Celsius |
| dpm | Disintegrations per minute |
| µm | Micrometer |
| cm | Centimeter |
| g | Gram |
| km | Kilometer |
| ka | Kilo-annum (Thousand years) |
| Ma | Mega-annum (Million years) |
| yr | Year |

# RÉSUMÉ

La chronostratigraphie de l'océan Arctique n'a pas encore été bien intégrée dans l'histoire du climat mondial en raison des chronologies conflictuelles qui ont été proposées jusqu'ici. L'absence de consensus est due en partie aux difficultés rencontrées pour dater les sédiments et déterminer les taux de sédimentation. Certaines de ces difficultés sont des taux de sédimentation bas et variables, le peu ou l'absence de restes biogéniques, les écarts entre les stratigraphies des isotopes de l'oxygène de l'océan local et en haute mer, et les interprétations conflictuelles des données paléomagnétiques. Dans ce contexte, l'extinction de l'excès de thorium 230 ($^{230}Th_{xs}$) dans les séquences sédimentaires peut servir à établir des balises temporelles sur des échelles glaciaires-interglaciaires allant jusqu'à ~ 375 ka. Ce radionucléide est utilisé dans cette situation depuis plus d'un demi-siècle, mais son utilisation n'a pas été généralisée et, pour l'océan Arctique, il y a toujours peu d'études utilisant la radiochronologie au-delà des limites temporelles du radiocarbone.

Nous examinons ici l'utilisation du $^{230}Th_{xs}$ comme outil stratigraphique dans une séquence sédimentaire du sud de la Ride de Lomonosov (PS2757) à laquelle on avait auparavant attribué des chronologies incompatibles en utilisant différentes méthodes. Selon les données $^{10}Be$ antérieures, la séquence est caractérisée par des vitesses de sédimentation significativement plus élevée que celles observées dans l'océan Arctique central. En se basant sur l'attribution de la base d'un pic de $^{230}Th_{xs}$ à ~ 520 cm à la transition MIS 7/8 (~ 243 ka), une vitesse moyenne de sédimentation de 2,1 cm/ka a été calculée. C'est un ordre de grandeur supérieur à celui des sites où la méthode $^{230}Th_{xs}$ a été utilisé avec succès auparavant.

La vitesse moyenne de sédimentation élevée est attribuable au transport de sédiments emportés par la dérive transpolaire à partir des plateaux continentaux de Laptev et de la Sibérie Orientale. Cependant, de grandes variations d'amplitude en $^{230}Th_{xs}$ sont superposées à la tendance à la décroissance exponentielle du haut vers le bas de la séquence. Elles suggèrent des intervalles avec une sédimentation et une récupération réduite de $^{230}Th$ dans la colonne d'eau, alternant avec des "excursions" de $^{230}Th_{xs}$, l'une, notamment, attribuée au stade isotopique 3, excursion également enregistrée dans plusieurs autres carottes de l'océan Arctique. La séquence étudiée possède une caractéristique particulière, à ~ 6 m de profondeur, illustrée par une importante mobilité diagénétique de l'uranium, en relation avec la teneur en carbone organique et les conditions redox. La mobilité de U est démontrée par les variations du $^{230}Th_{xs}$ et du rapport d'activité $^{234}U/^{238}U$ dans un intervalle autrement caractérisé par des équilibres quasi séculaires entre les inventaires de ces isotopes.

Il est conclu que la méthode du $^{230}Th_{xs}$ pour l'établissement de repères chronostratigraphiques dans les séquences de l'océan Arctique peut être utilisée pour un large éventail de taux d'accumulation de sédiments, à condition que les effets diagénétiques liés aux gradients redox dans la colonne sédimentaire ne modifient ni ne fractionnent la distribution des isotopes de la série de l’uranium.

Mots-clés : Océan Arctique, Ride de Lomonosov, Quaternaire, $^{230}Th_{xs}$

# CHAPTER I

# $^{230}$Th-EXCESS INSIGHTS INTO SEDIMENTATION RATES AND DIAGENETIC PROCESSES IN A LATE QUATERNARY SEQUENCE FROM THE SOUTHERN LOMONOSOV RIDGE, ARCTIC OCEAN

Karl Purcell [1], Claude Hillaire-Marcel [1], Anne de Vernal [1],
Bassam Ghaleb [1], and Rüdiger Stein [2]

[1] GEOTOP-UQAM, CP 8888 Montréal, H3C 3P8, Canada
[2] Alfred Wegener Institute for Polar and Marine Research, Bremerhaven, Germany

# ABSTRACT

The Arctic Ocean's chronostratigraphy has yet to be well integrated in the global climate history due to confllictingchronologies that have been proposed so far. The lack of consensus is partly due to difficulties encountered in dating sediments and determining sedimentation rates. Some of these difficulties are the slow and variable sedimentation rates, discrepancies between local and open ocean oxygen isotope stratigraphies, and conflictual interpretations of paleomagnetic data. In this context, the extinction of $^{230}$Th-excesses ($^{230}Th_{xs}$) in sedimentary sequences may provide the means to set time-constraints over glacial-interglacial timescales up to ~ 375 ka. This radionuclide has been used in this situation for over half a century, however its use was not widespread and there remains a paucity of studies using radiochronology past the temporal limits of radiocarbon.

Here we document the use of $^{230}Th_{xs}$ as a stratigraphic tool in a cored sequence from the southern Lomonosov ridge (PS2757) that had previously been given incompatible chronologies using different methods. According to earlier $^{10}$Be-data, the sequence is characterized by sedimentation rates significantly higher than those observed in the central Arctic Ocean. Based on the assignment of the end of a $^{230}Th_{xs}$ peak at ~ 520 cm to the MIS 7/8 transition at ~ 243 ka, an average sedimentation rate of 2.1 cm/ka was calculated. It is an order of magnitude above that of sites where the $^{230}Th_{xs}$ method was previously used.

The high average sedimentation rate is attributable to the transport of ice rafted sediments from the nearby Siberian and Laptev sea shelves by the Transpolar Drift. However, large amplitude variations in $^{230}Th_{xs}$ are superimposed on the exponential decay trend downcore. They suggest intervals with reduced sedimentation and $^{230}$Th-scavenging in the water column, alternating with $^{230}Th_{xs}$ "excursions", in particular a recent one attributed to the Marine Isotope Stage 3, also recorded in several other cores from the central and marginal Arctic Ocean.

PS2757 depicts a particular feature, at ~ 6 m downcore, illustrated by an important diagenetic mobility of uranium, in relation with organic carbon content and redox conditions. The U-mobility is documented by $^{230}Th_{xs}$ and in $^{234}U/^{238}U$ activity ratio variations within an interval otherwise characterized by near secular equilibria between inventories of these isotopes.

It is concluded that the $^{230}Th_{xs}$-approach for the setting of chronostratigraphic benchmarks in Arctic Ocean sequences can be used within a wide range of sediment accumulation rates, providing that diagenetic effects linked to redox gradients within the sedimentary column do not alter and fractionate the distribution of U-series isotopes.

Keywords : Arctic Ocean, Lomonosov Ridge, Quaternary, $^{230}Th_{xs}$

## 1.1. INTRODUCTION

The Arctic Ocean plays a major role in the Earth's climatic processes, in particular through the albedo effect of sea ice, and the impacts of freshwater fluxes on thermohaline circulation (Polyak, 2004; McPhee et al., 2009). Its role on the long-term can be documented by reconstructing past changes that are recorded in marine sedimentary archives. However, the setting of a robust chronostratigraphy of central Arctic Ocean sequences remains a challenge due to many factors such as difficulties in securing samples, low sedimentation rates and poor preservation of calcareous microfossils (e.g. Backman et al., 2004; Moran et al., 2006; Stein et al., 2008; Polyak et al., 2009).

There is an existing radiocarbon chronostratigraphy spanning late glacial and Holocene intervals which shows sedimentation rates ≤ 1 cm/ka in a number of cores from the central Arctic (Not and Hillaire-Marcel, 2010; Hillaire-Marcel et al., 2017) and up to a few cm/ka closer to the continental margin (e.g., Darby et al., 1997; Nørgaard-Pedersen et al., 2003; Stein et al., 2003; Polyak et al., 2004, Deschamps et al., 2018). This data also points to highly variable sedimentation rates during glacial periods, faster during massive iceberg discharges and much lower with hiatuses during the last glacial maximum (Darby et al., 2006; Not and Hillaire-Marcel, 2010; Polyak and Jakobsson, 2011).

However, the radiocarbon chronostratigraphy is limited to ages younger than 35 ka, as radiocarbon data from marine biogenic carbonates are often unreliable beyond this range (Backman et al., 2004; O'Regan, 2008; Polyak et al., 2009)

Beyond the limits of the $^{14}C$ dating-method, and due to the difficulties in correlating the $\delta^{18}O$-stratigraphy, the stratigraphy of the late Quaternary Arctic sediments is largely based on paleomagnetism. A stratigraphic layer extended across the Arctic Ocean has a slight magnetic inclination. This layer was initially interpreted as the boundary between the current Brunhes period and the Matuyama period (0.78 Ma) (e.g., Clark et al., 1980; Poore et al., 1993). Age constraints from $^{14}C$ and $^{230}Th$ were in agreement with this magnetically derived stratigraphy (Clark et al., 1986; Huh et al., 1997). The low sedimentation rates were also consistent with an analysis that linked sediment parameters to orbital variations in the earth (Boyd et al., 1984) and a study of the mechanics of sediment transport by ice (Clark and Hanson, 1983).

The paleomagnetic data were re-interpreted, assigning an age of 60 ka (Jakobsson et al., 2000, 2001; Backman et al., 2004) to the paleomagnetic reversal previously assigned to the Brunhes-Matuyama boundary (Lovlie et al., 1986). Amino acid ratios and their $^{14}C$-ages, cyclostratigraphy inferences, biostratigraphy correlations with sequences yielding reliable oxygen isotope records in the Fram Strait area, were used to support this revised stratigraphy leading to infer relatively high sedimentation rates in the central Arctic Ocean ($\geq 1$ cm/ka).

In view of this debate, the use of long-lived radioisotopes could provide means to set a more reliable stratigraphy for the Arctic Ocean. For instance, Dipre et al. (2018) dated sediments on the Northwind Ridge by strontium isotope stratigraphy, revealing that the previous chronostratigraphy that was based on counting lithostratigraphic layers, had grossly underestimated the age of the sediments. Another example that relates to the present study is that by using the distribution and inventories of $^{230}Th$-excesses ($^{230}Th_{xs}$) and $^{231}Pa$-excesses in very low sedimentation rate sites of the central Arctic Ocean, Not and Hillaire-Marcel (2010) and Hillaire-Marcel et al. (2017), demonstrated that the earlier stratigraphy set on the Brunhes-Matuyama boundary (Doell and Dalrymple, 1966; Spell and McDougall, 1992), with mm/ka sedimentation rates, was more likely than the stratigraphy with sedimentation rates over 1 cm/ka that had been used since Jakobsson et al. (2000) and is still used in many papers.

Figure 1.1 shows a simplified scheme of the creation and transport of $^{230}$Th in the water column. Thorium 230 is uniformly produced by uranium 234 dissolved in the water column. Being particle-reactive, $^{230}$Th is quickly removed from the water column though its scavenging by settling particles (e.g., Rosholt et al., 1961; François et al., 2004). The scavenged $^{230}$Th leads to $^{230}$Th-excesses ($^{230}$Th$_{xs}$) in the sediments, i.e., to $^{230}$Th activities in excess of those of parent $^{234}$U in the sediments (Rosholt et al., 1961). This excess depends on the production of $^{230}$Th in the water column, thus on i) the depth of the water column, ii) $^{230}$Th-scavenging processes by particles and sedimentation rates. It is also dependent of the age of the sediments, $^{230}$Th being itself subject to radioactive decay.

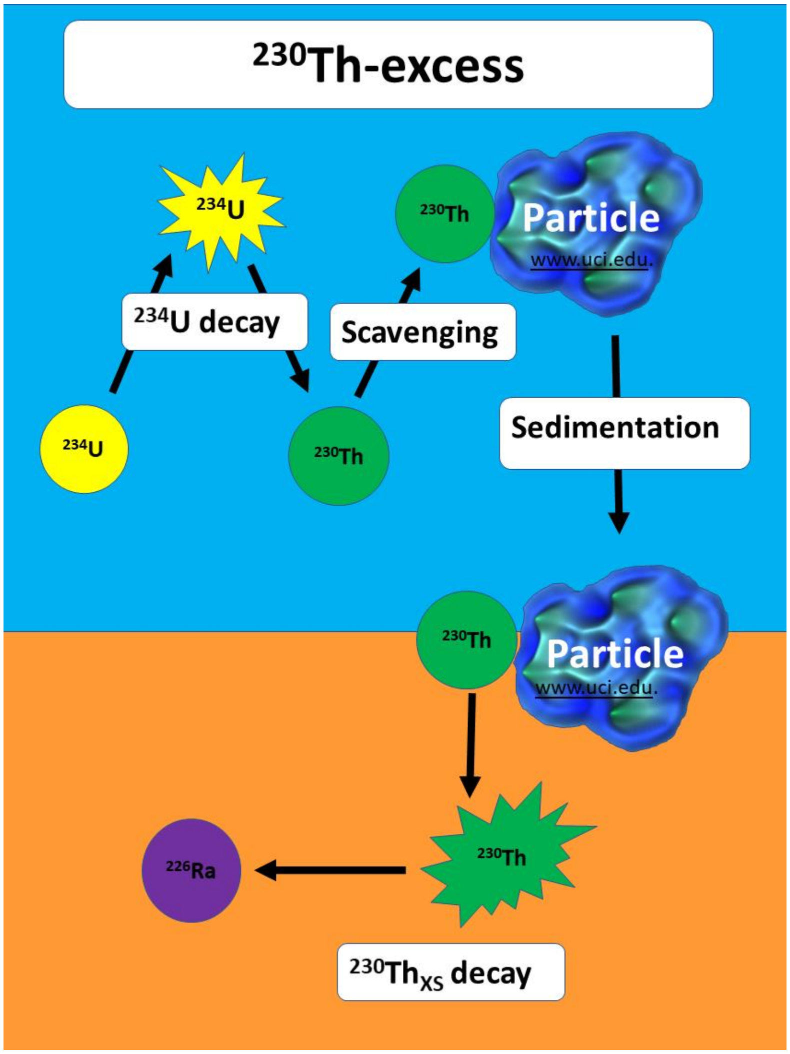

**Figure 1.1.** Simplified scheme of the creation, scavenging, and sedimentation of $^{230}$Th in the water column, and its subsequent decay in the sediments.

When $^{230}\mathrm{Th}_{\mathrm{xs}}$-activities decreases downcore below the quadratic sum of errors of $^{230}$Th vs parent $^{234}$U activities, the $^{230}\mathrm{Th}_{\mathrm{xs}}$ "clock" stops. In general, the quadratic sum of errors corresponds to a few per cent of the initial $^{230}\mathrm{Th}_{\mathrm{xs}}$, i.e., a $^{230}\mathrm{Th}_{\mathrm{xs}}$ which underwent a decay of about 4 to 5 times the half live of the isotope (75,690 years; Cheng et al., 2000). Thus, the "extinction age" of the $^{230}\mathrm{Th}_{\mathrm{xs}}$ in cored sedimentary sequences may be assigned an age of the order of ~ 300-375 ka in a first approximation (Hillaire-Marcel et al., 2017).

In high sedimentation rate sites, $^{230}$Th scavenged in the water column is mixed with large amounts of sediment. This results in $^{230}$Th excesses too low to allow estimating precisely the "extinction age" of the initial excess. Moreover, even discrete diagenetic processes may blur the theoretical exponential decay of $^{230}$Th$_{xs}$. Another important limitation of this approach is the content of organic carbon at the sea floor, leading to large amplitude redox gradients in the sedimentary column. These may result in a post-sedimentary redistribution of redox-sensitive elements such as U, while $^{230}$Th would not be affected but for its radioactive decay (Bonatti et al., 1971; Vallières, 1994). Therefore, the $^{230}$Th$_{xs}$ method has been proposed so far for organic carbon-poor, very low sedimentation sites of the central Arctic Ocean (on the order of mm/ka; Hillaire-Marcel et al., 2017).

Here we examine the distribution of $^{230}$Th$_{xs}$ in two sediment cores from the southern Lomonosov Ridge cores PS2757-8 and PS2757-6, raised from two relatively close stations. This study aims at testing the applicability of the $^{230}$Th$_{xs}$ method at sites with higher sedimentation rates than those where this method was previously used. Higher sedimentation rates are also expected to document better the temporal variability in fluxes of scavenged $^{230}$Th in relation with paleoceanographic changes. Aside from these objectives, the setting of a $^{230}$Th$_{xs}$-derived chronostratigraphy at the study sites from the periphery to the central Arctic Ocean, will be useful in the absence of radiocarbon and $\delta\,^{18}$O stratigraphies.

## 1.2. Physical setting of the Lomonosov ridge

### 1.2.1. Regional geology:

Grantz et al. (2010) describe the Lomonosov Ridge as a fragment of continental crust that, according to magnetic data, was split from the Barents continental shelf around 58 Ma. ago. It rises from the bottom of the Arctic Ocean to within 500 m of sea level, is 45 to 150 km wide, and goes from Russia to Greenland passing through the North Pole (figure 1.2. and 1.3.). It thus divides the Arctic Ocean in two, the Amerasian and Eurasian basins.

### 1.2.2. Main oceanic circulation:

In the Amerasian basin, the surface water circulates in the Beaufort Gyre (figure 1.2.), while over the Lomonosov Ridge, the Transpolar Drift moves from Russia's continental shelf to Fram Strait east of Greenland. These surface currents are largely driven by surface winds that have two main regimes (Proshutinsky and Johnson, 1997). These regimes can be linked to the Arctic Ocean oscillation (AOO) index, which is a very strong indicator of circulation changes and freshwater content in the Arctic Ocean (WHOI, 2019). When the AOO is negative, low atmospheric pressure at sea level is predominant over the central Arctic Ocean, and the surface winds cause the sea ice to drift counterclockwise. This is accompanied by a stronger Transpolar Drift and export of sea ice through Fram Strait

Conversely, when the AOO is positive, the sea level atmospheric pressure is higher, with surface winds that entrain the sea ice to drift clockwise in the Arctic Ocean. During those periods of positive AOO, there is a strengthening of the Beaufort Gyre, the gyre then being able to reach the Lomonosov Ridge. Additionally, in those time intervals freshwater accumulates in the Beaufort Gyre, which reduces the transport of freshwater towards the North Atlantic Subpolar Region, causing a reduction in stratification of the surface water masses and consequently an increase in deep convection.

Lastly, Morison et al. (2012) confirmed that runoff of major Eurasian rivers such as the Yenisei, Ob, and Lena have an important influence on the freshwater fluxes in the Arctic Ocean. The trajectories taken by the runoff are affected as well by the atmospheric circulation regimes.

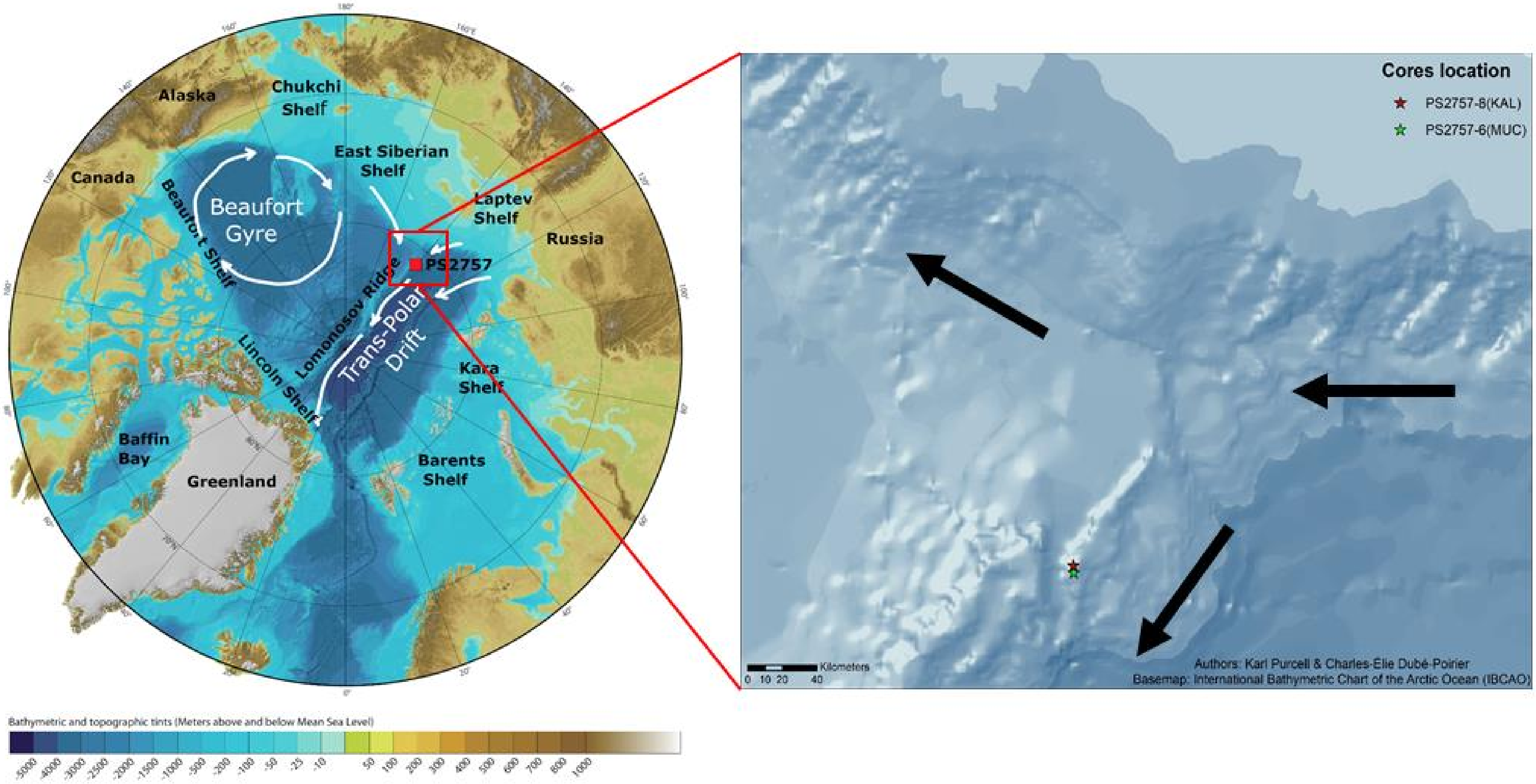

**Figure 1.2.** A) PS2757 cores location from Polarstern Cruise ARK-XI/1, Lomonosov Ridge (Arctic Ocean), 1995, and schematic illustration of the main surface currents in white. B) Close up showing the location of cores PS2757-8(KAL) and PS2757-6(MUC) with black arrows representing depth-averaged current directions (Woodgate et al., 2001). Background maps from Jakobsson et al. (2012).

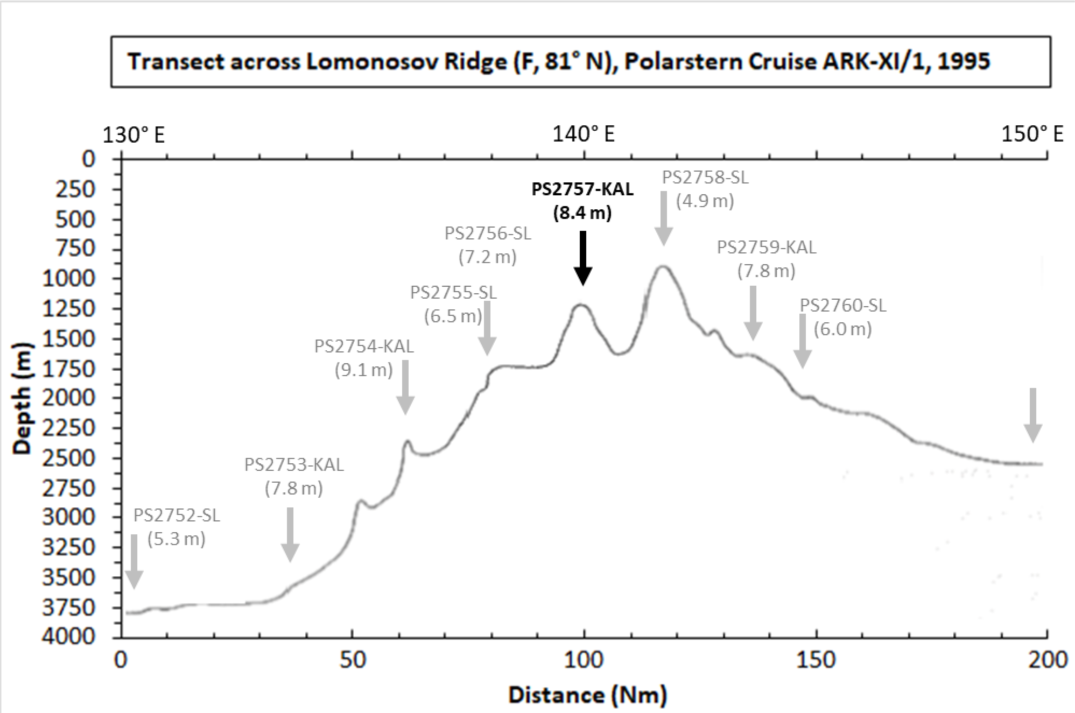

**Figure 1.3**. Transect across Lomonosov Ridge (F, 81°N) during the Polarstern expedition ARK-XI/1 in 1995 and location of core PS2757-8(KAL) indicated by black arrow. Numbers in parenthesis indicate core lengths in meters. Modified from Rachor (1997).

### 1.2.3. Sedimentology of the Lomonosov Ridge:

The study sites lie on the Lomonosov Ridge, near the Russian continental shelf (Figure 1.2). Because these sites are close to their principal sediment source, i.e, the Siberian and Laptev sea shelves, they are expected to receive a higher amount of sediments than sites near the North Pole (Fahl and Nöthig, 2007). A major portion of the sediments are brought to the sites by the Transpolar Drift which circulates over the ridge and carries sediments-laden sea ice. Those sediments are incorporated in sea ice during its formation over the Laptev and East Siberian shelves, from October to April (Reimnitz et al., 1994). This mechanism of transport is confirmed by Eicken et al. (1997, 2000), who found that sediment export by sea ice from the Laptev sea range 2 to 11 x $10^6$ tons of sediments per year, which is on the same order of magnitude as sedimentation in the Eurasian Arctic and Greenland Sea.

The sediments originate mainly from coastal erosion; Semiletov et al. (2011) reports that around 40 to 70 million tons of coastally eroded sediments are transported to the Laptev sea and East Siberian sea. Part of sediments deposited over the Lomonosov Ridge may also originate from land drainage by major Siberian rivers, the principal one being the Lena (Fahl and Nöthig 2007). It is possible that during glacial intervals the influence of coastal erosion was reduced, and thus the influence of rivers might have been proportionally higher, because there was less submerged continental shelf to be subjected to erosion. Alkama et al. (2008) found indications that during the LGM major Siberian rivers continued to flow into the Arctic Ocean through some rerouting around the Fennoscandian ice sheet.

The uppermost 48 cm of core PS2757-8 are composed of dark brown silty clay, while the sediments below are mostly an alternation of grayish brown, olive brown or dark brown, and dark gray silty clays. The dark gray layers are associated with higher amounts of sand. The brown layers are bioturbated, and some portions are laminated. The core contains occasional trace amounts of biogenic components such as foraminifers and coccoliths (Rachor et al, 1997).

### 1.2.4. Previous work on the study sites:

The core PS2757-8 was previously analyzed by Strobl (1998). Based on $^{230}Th_{xs}/^{10}Be$ ratios, a mean sedimentation rate of about 1.59 cm/ka was inferred. By contrast, Matthiessen et al. (2001) estimated an average sedimentation rate of 5-7 cm/ka downcore by extrapolating near surface microfossils maxima assigned to specific intervals and using a few$^{14}C$ ages. Finally, Stein et al. (2017) proposed a mean sedimentation rate of ~ 4.80 cm/ka based on correlations with other Arctic sequence, this time, using the cyclostratigraphy of Jakobsson et al. (2000), leading to attribute the 7.3 to 5 m downcore section to the MIS 6 to MIS 5e intervals. An independent assessment of the effective sedimentation rate at this coring site was thus much needed.

Based on evidence of ice scouring near core PS2757-8 that were dated at MIS 6 in nearby cores PS87/086-3, Stein et al. (2017) deduced the study site was under an extended ice shelf anchored in the East Siberian Ice Sheet. Following this episode, Stein et al. (2017) used biomarkers to infer the presence of an open water polynya between the Siberian Ice Sheet and the sea ice edge. This episode was followed by a rapid retreat of the ice sheet accompanied with high amounts of ice rafted debris (IRD) from calving icebergs and, finally, by a period of sea ice cover over the site with open waters towards the shelf during MIS 5e.

## 1.3. Materials and Methods

Core PS2757-8 (81°09.8′ N, 140°12.0′ E, 1241 m depth) was taken with a Kastenlot corer (KAL) while core PS2757-6 was retrieved nearby with a multicorer (MUC) during the Polarstern expedition ARK-XI/1 in 1995 (Rachor et al., 1997). The upper 25 cm of core PS2757-8 are missing. Therefore, core PS2757-6 was used in order to set a composite record of the study sites.

### 1.3.1. Samples and sediment characteristics:

Sedimentological, mineralogical, geochemical and micropaleontological properties of core PS2757-8 were available from earlier studies (Niessen, 1996; Müller and Stein, 2000; Matthiessen et al., 2001; Schoster, 2005). Müller and Stein, (2000) made grain size measurements using sieving/settling techniques and bulk sediment mineralogical analysis by X-ray diffraction. Wet bulk density changes downcore are from Niessen (1996) and were determined with a non-destructive Density Measuring System. Elemental geochemistry is from Schoster (2005). The measurements were made by X-ray fluorescence, except for sulfur which was analyzed with an elemental analyser. Micropaleontological analysis was done by Matthiessen et al. (2001).

### 1.3.2. Elemental (Ctotal, Corg, Ntotal) and stable isotope ($\delta^{13}C$) analysis

Total carbon, organic carbon and nitrogen contents were measured using a Carlo Erba™ elemental analyzer. A second aliquot was analysed for the organic carbon content after fumigation with HCl 12M to dissolve carbonates (in particular detrital dolomite; e.g., Maccali et al., 2013). The inorganic carbon content ($C_{inorg}$) was calculated by subtracting organic carbon to total carbon content. The isotopic composition of organic carbon was analysed on a fumigated aliquot with a Vario™ micro cube elemental analyser connected to an Isoprime 100™ mass spectrometer. Carbon-13 was calculated against VPDB, on the NBS19-LSVEC scale (Coplen et al., 2006), using 2 home reference materials ($\delta^{13}C$ = -28.73 ± 0.06‰ & -11.85 ± 0.04 ‰; Hélie, 2009). A 3rd reference material ($\delta^{13}C$ = -17,04 ± 0,11 ‰) was analyzed as an unknown to assess the exactness of the normalization. Results are given in delta units (δ) in ‰. Analytical precision is ± 0.1‰ for $\delta^{13}C$ (± 1σ) based on measurements of replicate samples.

### 1.3.3. U- and Th-series analyses:

For the purpose of the present study, 1 cm-thick subsamples of cores PS2757-6 and PS2757-8 from selected depths, with a 20 cm average interval, were obtained from AWI. Core PS2757-6 subsamples were received from the MARUM archives already dried, whereas those from PS2757-8 were dried at Geotop (at 70 °C during 24 h). All subsamples were then ground in an agate mortar. U-and Th-series analyses were done following procedures described in Edwards et al., (1987). The sediment was spiked by a solution containing know amounts of $^{233}U$, $^{236}U$ and $^{229}Th$ (46.88, 46.00, and 11.54 pmol/g, respectively). It was then digested by aqua regia, then by HF and $HNO_3$ before neutralization of HF by $H_3BO_3$ in HCl. U and Th separation was conducted on an anion exchange column (AG 1X8). Elution of U was done with HCl 6M and for Th, with HNO3 7M (Edwards et al., 1987). The Th fraction was purified on AG 1X8 columns while the U fraction was purified on UTEVA columns. Measurements of the U and Th isotopes were made on a MC-ICP-MS (Nu Plasma II™) at GEOTOP by peak jumping on a filtered ion counter. Mass bias is corrected from the $^{236}U/^{233}U$ ratio, while the standard HU-1 was used to monitor each analytical session. Replicates were performed on 6 samples and were statistically identical within ~ ± 1 % uncertainty, and blank values are negligible compared to the average uranium and thorium content of samples (blanks < 25 pg for U and < 150 pg for Th; Pons-Branchu et al., 2005). Results are quoted at ± 2σ uncertainty level. The U and Th isotopic concentrations were converted into activities with the half-lives taken from Cheng et al. (2000). Inventories of U-series isotopes were calculated in the following manner:

$$\text{Inventory (dpm/cm}^2\text{)} = \sum_{i}^{n} X_n(\text{cm}) \text{ x } \overline{A_n}(\text{dpm/g}) \text{ x } \overline{\rho_n}(\text{g/cm}^3)$$

Where $X_n$ is the thickness, $\overline{A}_n$ the average activity, and $\bar{\rho}_n$ the average dry bulk density of the N$^{th}$ depth interval between sampled depths (Not and Hillaire-Marcel, 2010). Between the measured depths, all values were linearly interpolated.

In marine sediments there are three sources of $^{230}$Th: $^{230}$Th$_{xs}$ scavenged from the water column, detrital $^{230}$Th (i.e., produced by uranium present in detrital grains), and authigenic $^{230}$Th, which is produced by the decay of authigenic U precipitated at the water/sediment interface (Anderson et al., 1990). Here we did not use the approach of Lao et al. (1993) to calculate $^{230}$Th$_{xs}$; only scavenged and detrital $^{230}$Th were taken into account. Authigenic $^{230}$Th was deemed to be negligible because the activity of $^{234}$U and $^{238}$U is nearly equal, having an average $^{234}$U/$^{238}$U AR in the top 560 cm of 0.987 ± 0.029 dpm/g (± 1σ). This suggests that there was no significant uptake of uranium from pore water, since the $^{234}$U/$^{238}$U AR is 1.1434 ± 0.0036 in Arctic Ocean waters (Not et al., 2012). Furthermore, the sediments were mostly deposited under oxidizing conditions, as inferred from the low organic carbon content and by the absence of an increase in U concentration downcore as found by Bonatti et al. (1971) and further observed here. The $^{230}$Th$_{xs}$ is thus calculated by measuring total $^{230}$Th activity and subtracting $^{238}$U activity, the latter being a proxy for detrital $^{230}$Th. It is assumed that detrital $^{230}$Th and $^{238}$U are in secular equilibrium. $^{238}$U activity is used here instead of that of $^{234}$U, the latter being the direct parent of $^{230}$Th. It will be shown below that $^{238}$U activity is less affected by diagenetic mobility of uranium in the sediments than that of its daughter $^{234}$U, and thus provides a better proxy-value of the activity of the supported $^{230}$Th fraction.

When the difference between $^{230}$Th$_{xs}$ and $^{230}$Th$_{supported}$ falls within the quadratic sum of the error bars (here ± 2 σ), there is no more measurable excess left with a 95 % probability. This depth is used here to define the limit of measurable $^{230}$Th$_{xs}$. The age of this depth is referred to as the “extinction age” of $^{230}Th_{xs}$. Ideally, this approach would require a constant flux in $^{230}Th_{xs}$ at the coring sites. Nevertheless, variations of $^{230}Th_{xs}$ are not critical for the setting of the $^{230}Th_{xs}$ extinction depth, as it simply corresponds to the depth where the difference between activities of $^{230}Th_{total}$ and $^{238}U$ fall within the quadratic sum of the corresponding error bars.

## 1.4. Results

### 1.4.1 Samples and sediment characteristics:

Density varies between ~ 0.49 and 1.33 g/cm$^3$ (Figure 1.12., and Tables 1.2 and 1.4) for core PS2757-8. This core is composed of mostly brown silty clay (Rachor et al., 1997) with intervals containing between 0 % and 30 % sand (Müller et al., 2000). Clay and sand contents are anticorrelated (R= -0.70; see figure 1.4). The alternance of silty and sand rich layers suggests variable depositional processes. There is a significant difference between the grain size fractions of sediments in the study core PS2757-8 vs those of core PS8730-030-3, located further away from the Russian continental margin. In the top 15 cm of core PS2757-8, the average weight percentages of sand, silt and clay are 3.5 %, 46.4 % and 50.1 %, respectively (Müller and Stein, 2000), whereas in core PS8730-03-3, they are 7.8 %, 75.2 % and 17.0 %, respectively (Le Duc, 2018). This difference can be explained by partly distinct sediment sources. As stated earlier, the study sites show sediments originating predominantly from the Russian continental shelves and transported by the TPD, whereas core PS87-030-3 contains at least in part, sediments originating from the western Canadian Arctic, carried along the Beaufort Gyre by sea ice (Le Duc., 2018).

In core PS2757-8, quartz (~ 43 %), plagioclase (~ 24 %), pyroxene (~ 10 %) and alkalifeldspars (~ 6 %) dominate, with variable minute amounts of amphibolites, kaolinites, chlorites, smectites and illites (Müller et al., 2000). Between 240 and 600 cm, the group of heavy minerals is dissimilar to adjacent sediments, suggesting that this interval contains sediments from a different source (Rachor et al, 1997).

In core PS2757-8, as documented by Matthiessen et al. (2001), peaks in dinocyst contents are observed at around 50 cm (*Operculodinium centrocarpum, Pentapharsodinium dalei*), and 220 cm (*Operculodinium centrocarpum*). Deeper downcore, dinocysts were practically absent, except for “single occurrences of *Nematosphaeropsis labyrinthus* cysts at 645- and 76.5-cm core depth”.

### 1.4.2 Nitrogen, carbon, and $^{13}$C in organic carbon ($C_{org}$):

The nitrogen content [0.08 % ± 0.02 (± 1σ)] is low and little variable throughout cores PS2757-8 and PS2757-6, whereas the total and organic carbon content varies from 0.1 to 1.0 % (Figure 1.4 and table 1.2 and 1.4). $C_{org}$ content is peaking at ~ 2.3 m, and more importantly at ~ 6.9 m. As $C_{org}/N_{total}$ ratios ranges from 1.9 to 9.8 with an average of 3.5 and follow the $C_{org}$ pattern, organic matter fluxes are likely primarily linked to marine sources (see Stein et al., 1994) .

The $C_{total}$ and $C_{org}$ percentages were used to correlate core PS2757-6 with PS2757-8, in order to create a composite record (Figure 1.5). Both cores have nearly identical values at a depth of 25 cm (Table 1.2 and 1.4). This suggests a nearly identical sedimentation rate for both cores in the upper first 25 cm.

The isotopic composition of organic carbon ($\delta^{13}C_{org}$) averages -23.0 ± 0.4 ‰ (± 1σ) down to 6.24 m, and then reaches a negative peak of -25.1 ‰ centered at 6.94 m (Table 1.2 and 1.4). This negative peak coincides with the third peak in $C_{tot}$ and $C_{org}$ abundance. It suggest a pulse of continental organic carbon at this depth (see also Naidu et al., 2000).

### 1.4.3 U- and Th-series isotopes:

The [Th]/[U] molar ratio of the composite record averages 5.45 ± 1.01 (± 1σ), which is within the range observed in river particulate matter (3.67 ± 3.85 (± 1σ) ; Viers et al., 2009). Concentrations in uranium and thorium (Figure 1.4) display large variations, especially below ~560 cm, which could indicate some uranium mobility or major mineralogical composition changes.

Cumulative inventories of $^{234}$U and $^{238}$U down to the composite core bottom yielded an activity ratio -AR-($\sum(^{234}U)$ (dpm/cm$^2$) / $\sum(^{238}U)$ (dpm/cm$^2$)) of 1.015 ± 0.004 (± 1σ). The near secular equilibrium value suggests that no significant diagenetic marine uranium is present in the cored sedimentary column, since the $^{234}U/^{238}U$ AR activity ratio is 1.1434 ± 0.0036 in Arctic Ocean waters (Not et al., 2012).

$^{230}$Th excesses where calculated using $^{238}$U as a proxy for the supported fraction. $^{238}$U was used instead of the $^{234}$U because it has less variability in the composite core. The $^{230}$Th excesses display an exponential decay trend towards the bottom of the core, with large amplitude variations. These variations include four peaks centered at the surface, ~ 1 m, ~ 3 m, and ~ 4.5 m to be discussed later (Figure 1.4).

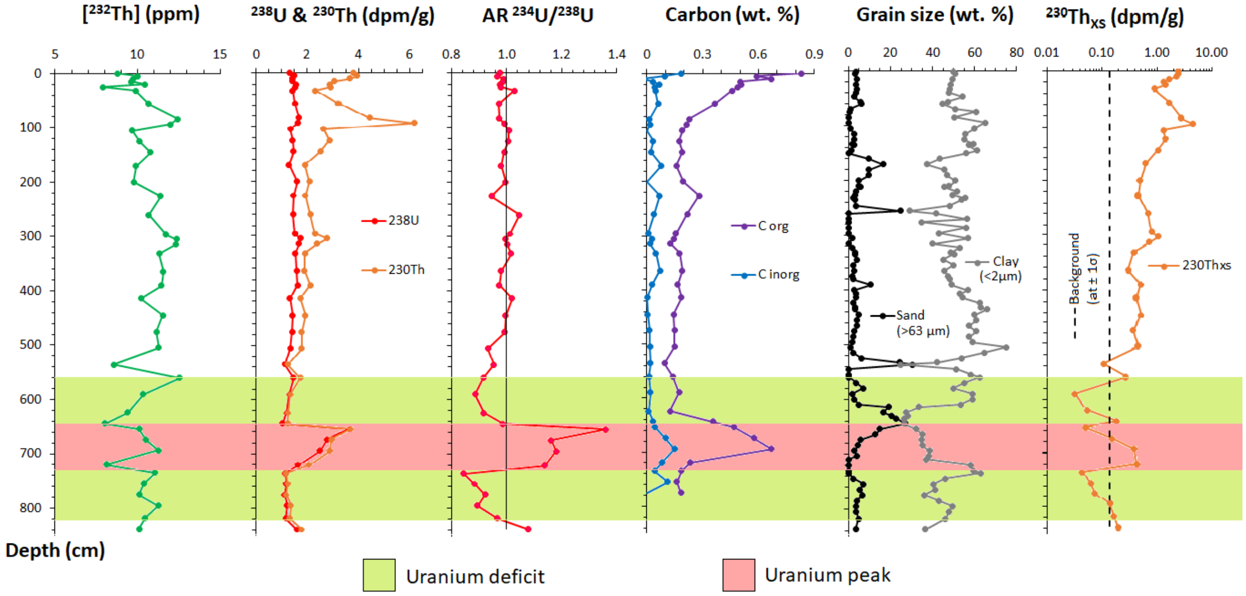

**Figure 1.4.** Geochemical and sedimentological composition of the composite core: Th and U contents, $^{234}U/^{238}U$ activity ratio, carbon content, grain size, and a log-plot of $^{230}Th_{xs}$ with the 1σ uncertainty on the supported fraction (cf. "background"). The red layer has a high uranium concentration, while the green layers have a low uranium concentration (high and low defied by a variation over 1σ). See tables 1.1. to 1.4.

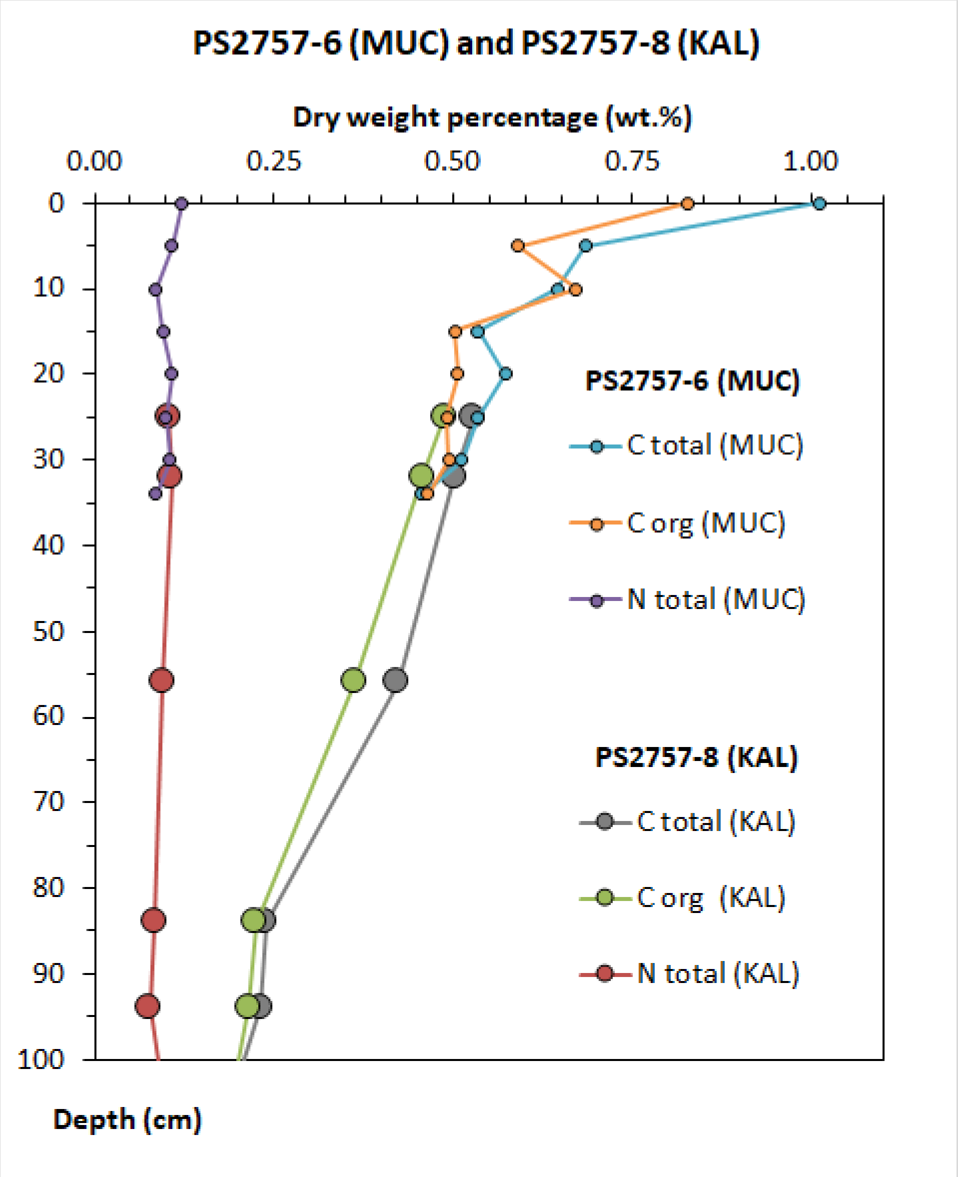

**Figure 1.5.** Ctot%, Corg% and N% vs. depth in cores PS2757-6(MUC) and PS2757-8(KAL). Both cores have nearly identical values at 25 cm and similar values on analyses below.

## 1.5. Discussion

As the objective of this study is to set a chronostratigraphy of the sequence using $^{230}Th_{xs}$, the first point of discussion concerns any post-depositional potential uranium mobility in the sediments.

### 1.5.1. U-mobility

As mentioned in the methodology, early diagenetic uptake of uranium is not considered since there is no enrichment in $^{234}U$ at core top that could be linked to diffusion and within pore water. Additionally, any significant inherited disequilibrium between $^{234}U$- and $^{238}U$ in the detrital fraction is discarded, at least down to 560 cm, as the $^{234}U/^{238}U$ activity ratio of this section is close to secular equilibrium (0.987 ± 0.029; ± 1$\sigma$). However, below 560 cm, late diagenetic U-mobility can be inferred, in view of the large amplitude variation of $^{238}U$-concentration [U] and $^{234}U/^{238}U$ activity ratio observed. A pronounced [U] peak is observed between ~ 650 and 720 cm. It is overlain and underlain by lower [U]-values (respectively between ~ 560-650 and ~ 730-820 cm). Contrasting with the unvarying $^{234}U/^{238}U$ activity ratio observed above 560 cm, the U-enriched horizon is matched by a strong excess in $^{234}U$ (AR$^{234}U/^{238}U$ up to 1.366 ± 0.014), whereas the U-depleted horizons are characterized by deficits in $^{234}U$ (AR$^{234}U/^{238}U$ as low as 0.843 ± 0.004) (see AR$^{234}U/^{238}U$ in Figure 1.4), illustrating the preferential mobility of $^{234}U$ vs $^{238}U$. Accordingly, $^{230}Th$ appears in strong excess in the U-depleted layers and in deficit in the U-enriched layer. This suggests a slow diagenetic process. As the U-peak with a strong excess in $^{234}U$ matches a relatively high content in organic carbon recorded between 654 and 694 cm ($C_{org}$ from 0.47 to 0.67 % compared to the core mean of 0.29 % ; Figure 1.4), U-leaching of detrital minerals in the over- and underlying layers, with preferential departure of $^{234}U$, and the subsequent $^{234}U$-enriched U-precipitation in the $C_{org}$-rich layer may reasonably be assigned to strong redox gradients between the oxidized U-depleted layers and the U-enriched horizon. Such post-depositional diagenetic processes have been observed along redox boundaries in turbidite sequences (Colley et al., 1984, 1989) and glacial/interglacial sedimentary sequences from the Labrador Sea (Vallières, 1997). In this latter case, worth of mention is the fact that the glacial oxidized layers show deficits of $^{234}$U (vs $^{238}$U) increasing with time, from an AR $^{234}$U-$^{238}$U ~ 0.90 (MIS 2), to AR $^{234}$U-$^{238}$U ~ 0.88 (MIS 4) and AR $^{234}$U-$^{238}$U ~ 0.85 (MIS 6), illustrating the long-duration of the redox-driven diagenetic U-relocation process.

Worth of attention is the fact that fluctuations in the concentration and isotopic ratio of uranium could also originate from other processes. For example, leaching of uranium with a bias toward $^{234}$U departure from detrital grains during their erosion and transport could result in $^{234}$U/$^{238}$U and $^{230}$Th/$^{238}$U activity ratios off secular equilibrium (Vallières, 1997; Vigier et al., 2001), while uptake of uranium from seawater would bring the $^{234}$U/$^{238}$U AR towards that of seawater (~ 1.144; Chen et al., 1986; 1.1434 ± 0.0036, Not et al., 2012). As mentioned above, core-top sediment properties discard any significant impact of these processes, at least, in recent time. Other potential processes to consider are i) sedimentary supplies originating from different bedrock sources, thus with distinct U-Th series signatures, varying through time, ii) inputs from peats and active layers of permafrost soils. Indeed, such deposits may present very high [U] and $^{234}$U/$^{238}$U AR ($^{234}$U/$^{238}$U AR up to 1.415 in samples from Bol'shoy Lyakhovsky Island in Russia, ~ 860 km south of the study sites, Schirrmeister et al., 2002; see also Allard et al., 2012). The fact that $\delta^{13}$C has a negative peak at the depth of the [U] peak is suggestive of an increased supply of terrigenous organic carbon. Therefore, one cannot discard the possibility that part of the U present in this layer and of its $^{234}$U-excess could relate to inland supplies, in opposition to the more important source of detrital sediments mobilized through coastal erosion.

In the present case, aside the late diagenetic U-relocation observed below 560 cm, most of the above processes seem to have been of reduced impact. On one hand, Th-concentrations [Th] vary only moderately within the whole sequence (10.6 ± 1.2 ppm; ± 1$\sigma$), as does the $^{238}U/^{232}Th$ AR in the diagenetically unaffected upper 560 cm (0.558 ± 0.048; ± 1$\sigma$; see tables in annex). On another hand, inventories of $^{234}U$ and $^{238}U$ throughout the whole sequence point to a mean activity ratio of 1.015 ± 0.004 (± 1 $\sigma$), which suggests that there was no major inherited disequilibrium, the two isotopes being essentially redistributed in the diagenetically impacted section below 560 cm, due to the low redox-high organic carbon peak centered at ~ 7 m downcore.

A closer look at $^{230}Th$ behaviour from 560 to 840 cm, further documents the diagenetic U-redistribution process. Inventories of excesses in $^{230}Th$ and $^{234}U$ vs $^{238}U$ below 560 cm indicate that $^{230}Th$ and $^{234}U$ depart only by 2.6 % from secular equilibrium (Figure 1.6). On one hand, this indicates that initial excesses in $^{230}Th$ vs $^{234}U$ are close to extinction below 560 cm. On another hand, it demonstrates that the diagenetic U-relocation process is mostly confined to this deeper layer. Whereas, above and below the U-relocation peak, the layers having loss some U do show excesses in $^{230}Th$ over parent $^{234}U$, these are practically balanced by the $^{230}Th$-deficit observed in the U-enriched layer itself. All together, inventories from $^{238}U$ to $^{230}Th$ show a nearly balanced budget within the diagenetically affected layer (Fig. 1.6), whereas the internal disequilibria record the time-dependence of the U-relocation process.

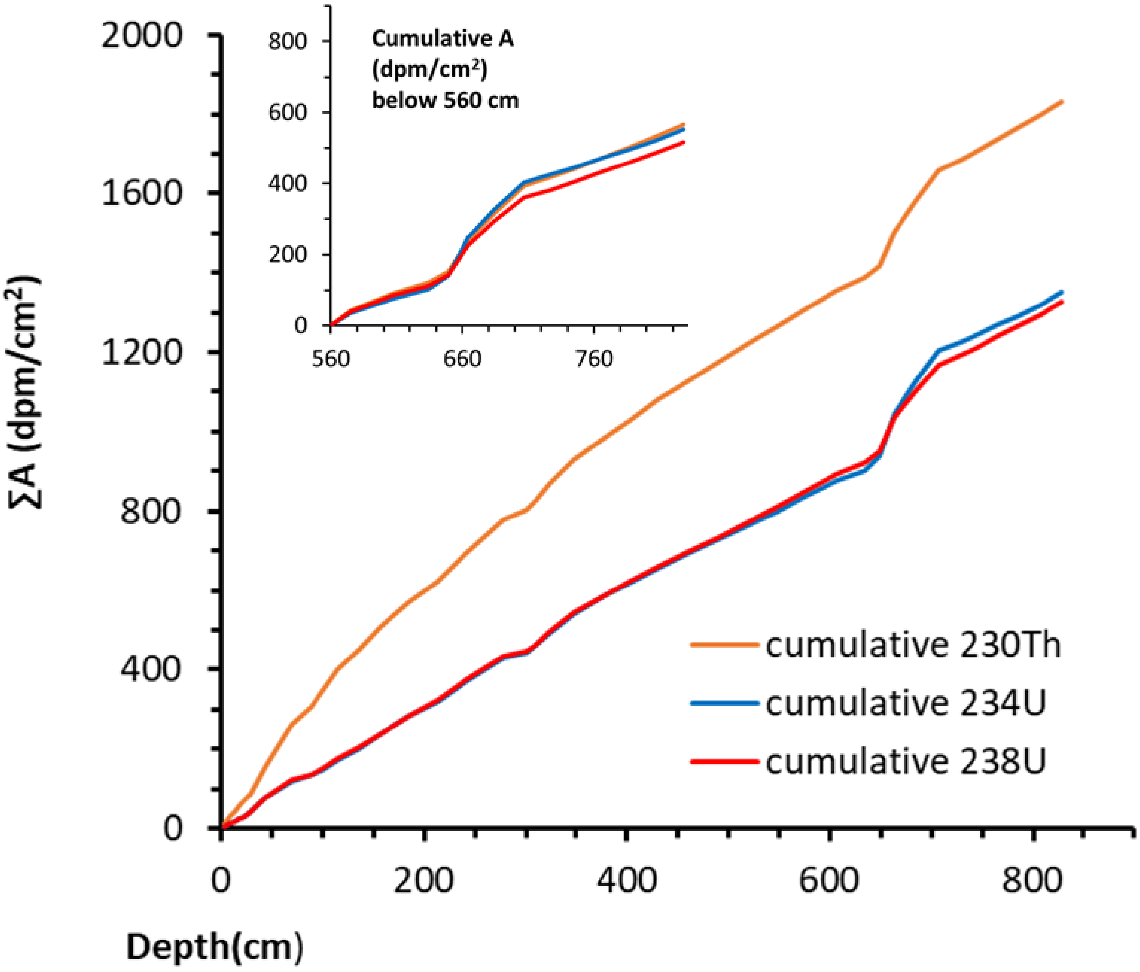

**Figure 1.6.** Cumulative activity of $^{230}$Th, $^{234}$U and $^{238}$U. In the upper corner, blow up of cumulative activities below 560 cm, i.e., i.e., from the depth of late U-diagenetic mobility. Within the interval 560-838 cm, the cumulative inventory of total $^{230}$Th is only 2.6 % higher than that of parent $^{234}$U, which is very close to error, thus pointing to near-global equilibrium conditions, thus the extinction of $^{230}$Th$_{xs}$ approximately at the 560 cm limit.

Using the $^{230}$Th/U age equation below (Ludwig, 2003), it is possible to give an estimate of the minimum age of mobility:

$$\frac{^{230}\mathrm{Th}}{^{234}\mathrm{U}} = \frac{^{238}\mathrm{U}}{^{234}\mathrm{U}}\left(1 - e^{-\lambda_{230}t}\right) - \left(1 - \frac{^{238}\mathrm{U}}{^{234}\mathrm{U}}\right)\left(\frac{\lambda_{230}}{\lambda_{234} - \lambda_{230}}\right)\left[1 - e^{(\lambda_{234} - \lambda_{230})t}\right]$$

The assumption is made that in the concerned layer the $\frac{^{234}\mathrm{U}}{^{238}\mathrm{U}}$ AR was initially equal to the top 560 cm. It is also assumed there was no mobility of Th and therefore the activity of $^{232}$Th can be used to calculate the initial activities of U-Th isotopes. The AR used in the calculations are for the added U-Th;

Where $^{238}\mathrm{U}_{\mathrm{added}} = {}^{238}\mathrm{U}_{\mathrm{peak}} - ( \frac{^{238}\mathrm{U}}{^{232}\mathrm{Th}}\mathrm{initial} * {}^{232}\mathrm{Th}_{\mathrm{peak}} )_1$,

$^{234}\mathrm{U}_{\mathrm{added}} = {}^{234}\mathrm{U}_{\mathrm{peak}} - ( \frac{^{238}\mathrm{U}}{^{232}\mathrm{Th}}\mathrm{initial} * \frac{^{234}\mathrm{U}}{^{238}\mathrm{U}}\mathrm{initial} * {}^{232}\mathrm{Th}_{\mathrm{peak}} )_2$,

and $^{230}\mathrm{Th}_{\mathrm{added}} = {}^{230}\mathrm{Th}_{\mathrm{peak}} - (\frac{^{238}\mathrm{U}}{^{232}\mathrm{Th}}\mathrm{initial} * \frac{^{234}\mathrm{U}}{^{238}\mathrm{U}}\mathrm{initial} * {}^{232}\mathrm{Th}_{\mathrm{peak}} )_3$.

(The terms 1, 2 and 3 are initial $^{238}$U, $^{234}$U and $^{230}$Th activities respectively. $^{230}\mathrm{Th}_{\mathrm{added}}$ was not displaced from neighboring layers but was produced by the decay of the added $^{234}$U )

The inventories of all isotope of concern within the U-enriched peak (~ 645-728 cm down composite core), yield the following activities: $^{238}$U = 259.0 ± 1.9 dpm (347 ± 2.5 μg) ; $^{234}$U = 313.4 ± 1.7 dpm; $^{230}$Th ~ 285.7 ± 1.1 dpm; $^{232}$Th ~ 252.9 ± 4.2 dpm (1036.1 ± 13.6 μg). For the initial AR: $\frac{^{238}\mathrm{U}}{^{232}\mathrm{Th}}\mathrm{initial} = 0.558 \pm 0.048$, $\frac{^{234}\mathrm{U}}{^{238}\mathrm{U}}\mathrm{initial} = 0.987 \pm 0.029$.

These inventories and initial AR allowed the calculations of the following results: $\frac{^{238}\mathrm{U}}{^{234}\mathrm{U}}\mathrm{added} = 0.677 \pm 0.088$, $\frac{^{230}\mathrm{Th}}{^{234}\mathrm{U}}\mathrm{added} = 0.841 \pm 0.095$, and an age of $169^{+39}_{-32}$ ka was obtained. However, this age is a minimum, as no added uranium was present at the beginning; the $^{230}$Th produced by the displaced uranium was in effect produced at a slower rate than if all the uranium was there at the start. This calculation gives a rough estimate of the diagenetic process leading to the disequilibria observed between $^{238}$U-$^{234}$U-$^{230}$Th in the U-enriched peak.

### 1.5.2. Production, transport and fluxes of $^{230}Th_{xs}$

Using a theoretical water column production of $^{230}$Th of about 2.63 $\frac{dpm.}{cm^2 x\ km\ x\ ka}$ (Lalou and Nguyen, 1985), notwithstanding fluctuations in sea level and salinity (thus of the dissolved U-concentration), as well as in the subsequent (minor) changes in the isotopic composition of this dissolved uranium (± 15 ‰ in the last 360 ka; Henderson, 2002), it is obvious that the effective $^{230}Th_{xs}$ inventory in the composite sequence is higher than the amount of $^{230}Th_{xs}$ theoretically produced in the overlying water column (482 vs 280 dpm/cm$^2$), as illustrated in figure 1.10 lower in the text. This implies significant boundary scavenging of the water column $^{230}$Th. Specific processes have been proposed in Moran et al., (2005) and Hillaire-Marcel et al. (2017). They involve redistributing the $^{230}$Th from the low productivity, ice covered interior basins towards shelves and slopes where it is scavenged due to seasonally high particle fluxes and frequent resuspension events (cf. boundary scavenging process in Anderson et al., 1990). In contrast, sedimentation over ridges from the Central Arctic Ocean is exclusively linked to low particulate fluxes linked to ice-rafting.

According to Edmonds et al. (1998) and Trimble et al. (2004) the main scavengers of $^{230}$Th in the Arctic Ocean are clay sized lithogenic particles transported by ice rafting. However, submicron colloidal matter such as dissolved organic carbon (DOC) plays a major role in scavenging $^{230}$Th (Moran et al., 1997; Baskaran, 2001; Maccali et al., 2019), while suspended particulate matter (SPM) plays a role as well (Trimble et al, 2004; Hoffmann et al., 2013). Another potential scavenging process is the adsorption of $^{230}$Th by Mn oxide coatings (e.g., Roy-Barman et al., 2009). In the studied sequence, as illustrated in figure 1.7, $^{230}Th_{xs}$ peaks coincide with relatively fine sediment accumulation intervals, i.e., with high scavenging capability, while $^{230}Th_{xs}$ valleys are associated with coarser sedimentats (high sand contents). The initial $^{230}Th_{xs}$ above 560 cm ($A_{initial} = A_{measured} \div e^{-\lambda \times t}$, where t is derived from the age model that assigns an age of 243 ka at a depth of 520 cm discussed below) shows some correlation (R = 0.59) with the clay-size content (< 2µm), suggesting that this sediment fraction is likely involved in the scavenging and transport of $^{230}Th_{xs}$ towards sediment surface. Figure 1.7 illustrates this link between $A_{initial}$ and clay content. The two parameters have coinciding peaks, but there is a decoupling that can be seen between the peaks that remains to be explained. Further sedimentological analysis could be done to explain this decoupling.

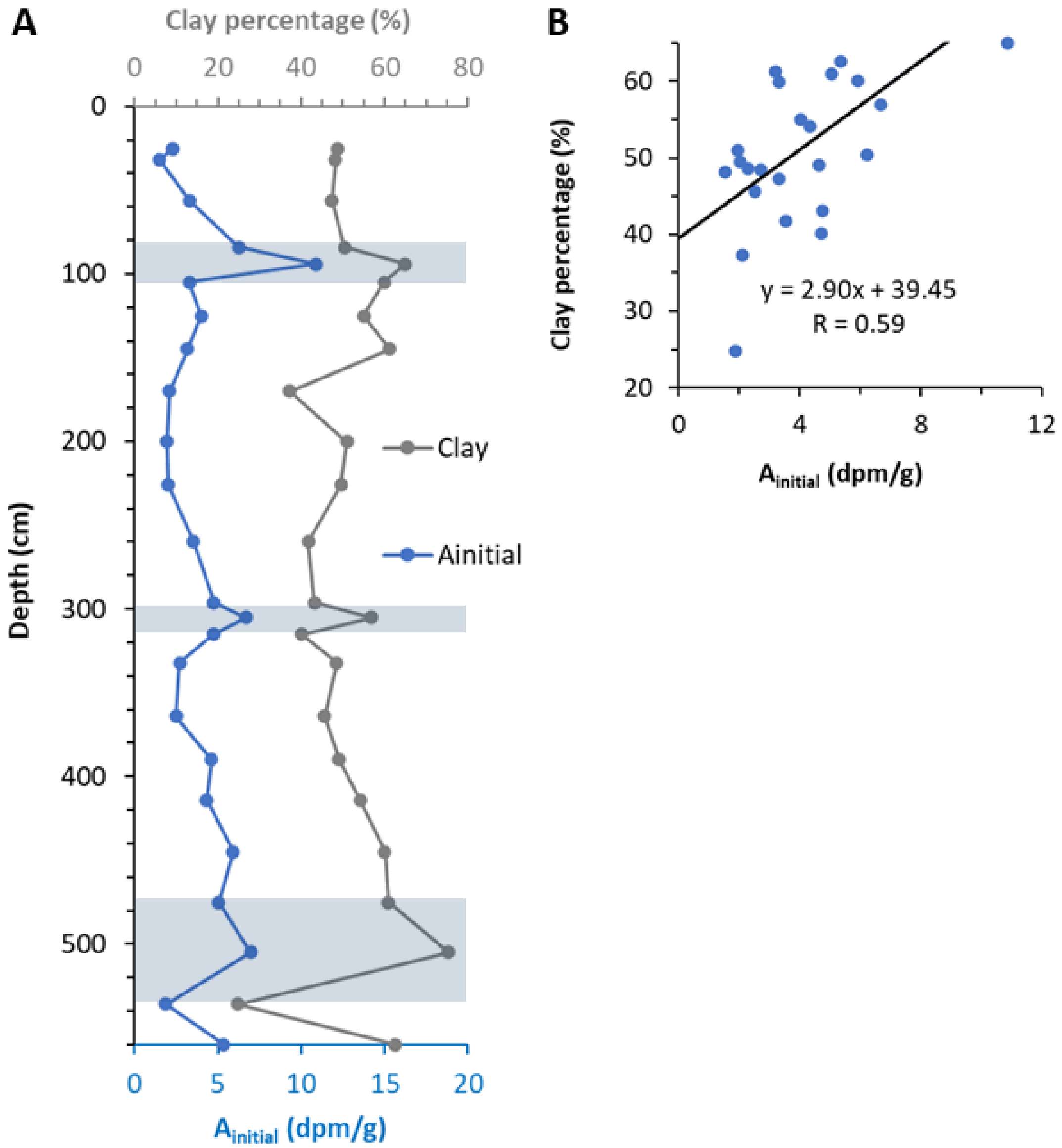

**Figure 1.7. A.** Clay-size sediment content (< 2µm) shown alongside initial $^{230}\mathrm{Th}_{xs}$ ($\mathrm{A}_{initial}$) above 560 cm in the composite core. Peaks coinciding in the two parameters are highlighted in blue. **B**. Clay-size sediment vs initial $^{230}\mathrm{Th}_{xs}$ with linear trend line.

The large amplitude variations of $^{230}\mathrm{Th}_{xs}$ vs the theoretical decay curve under steady state conditions, corresponding to constant sedimentation and constant $^{230}\mathrm{Th}_{xs}$ flux, can be assigned to glacial-stadial/interglacial-interstadial successions (Not and Hillaire-

Marcel, 2010). During glacials, Henderson et al. (1999) found little scavenging in the Arctic Ocean accompanied with export of $^{230}$Th to the North Atlantic by introducing a particle field into an ocean general circulation model.

Not (2010) found that throughout glacial-stadial intervals (MIS 2, MIS 4, and MIS 6) , there was less clay sized detrital sediments, and a higher input of coarser fraction brought by icebergs in the Central Arctic Ocean. Also, the absence of foraminifer shells during glacial intervals in sediment cores analyzed by Not (2010) indicates that there was less biological productivity, thus a less abundant supply of biogenic SPM and DOC in those intervals. Additionally, Not (2010) observed less carbonate sedimentation in those time periods, therefore there would have been a smaller supply of detrital carbonates for the formation of Mn oxide coatings that can adsorb $^{230}$Th. All of these elements would have resulted in a less efficient scavenging $^{230}$Th in the water column.

Conversely, Not (2010) found indications that during interglacial-interstadial periods (MIS 1, MIS 3, and MIS 5), there was higher biological productivity and carbonate sedimentation in the central Arctic Ocean. Moreover, higher amount of fine sediments transported by sea ice can be assumed because of a higher sea level and larger shelf area, where sediment resuspension and ice formation take place (Reimnitz et al., 1994). During interglacials and interstadials with increased fine sediment inputs, a more efficient scavenging of $^{230}$Th could have led to enhanced $^{230}$Th$_{xs}$ in the sediments (Hillaire-Marcel et al., 2017). The low content of coarse fraction sediments corresponding to high $^{230}$Th$_{xs}$ points to transport by ice rafting of sea ice rather than by icebergs. Another explanation invoked by Hillaire-Marcel et al. (2017) for the increase in $^{230}$Th$_{xs}$ during "warm" periods is an increase of $^{230}$Th carried by high density organic-rich brines. Higher sea level and larger shelf areas are favourable to sea ice formation and therefore rejection of brines, which may contain very high concentrations of scavenging particles, notably biological remains such as diatoms, faecal material, and aggregates (Michels et al., 2008; Thomas et al., 2008).

Another influence that can be explored is the sorting of the sediments as they settle by currents such as the Arctic Ocean boundary current. Woodgate et al., (2001) deployed moored instruments near the study sites (81°5.5’ N, 138°54.0’) and measured a yearly mean velocity of 1 to 2.4 cm/s at different depths, with peaks going up to 35 cm/s for 6-hour periods. Changes in past current speeds can be inferred from the sortable silt grain-size (McCave et al., 2017). However, concerns about the possibility that the sediments cannot be used for this purpose due to contamination by unsorted silts brought by ice rafting have to be addressed. Following McCave et al.’s methodology (2019), a 5-point running correlation between sortable silt mean and percentage ($\overline{SS}$ µm vs $\overline{SS}$ %) was calculated downcore to discriminate poorly sorted silts, with a value of $r < 0.5$ being the cut-off point. It can be seen in figure 1.8. that most of the sequence contains silts that are sufficiently sorted to deduce variations in paleocurrents, except for two intervals centered around 260 and 640 cm. Dips in inferred current speeds are observed at 4 depths that can be compared to peaks in excess $^{230}\mathrm{Th}$. This relationship could be explained: during periods of slower flow, there would be less winnowing of fine particles which are efficient scavengers of $^{230}\mathrm{Th}_{xs}$. The comparison is limited however, with the second dip in $\overline{SS}$ being in a poorly sorted interval, and the last peak of initial $^{230}\mathrm{Th}_{xs}$ being in the uranium mobility zone.

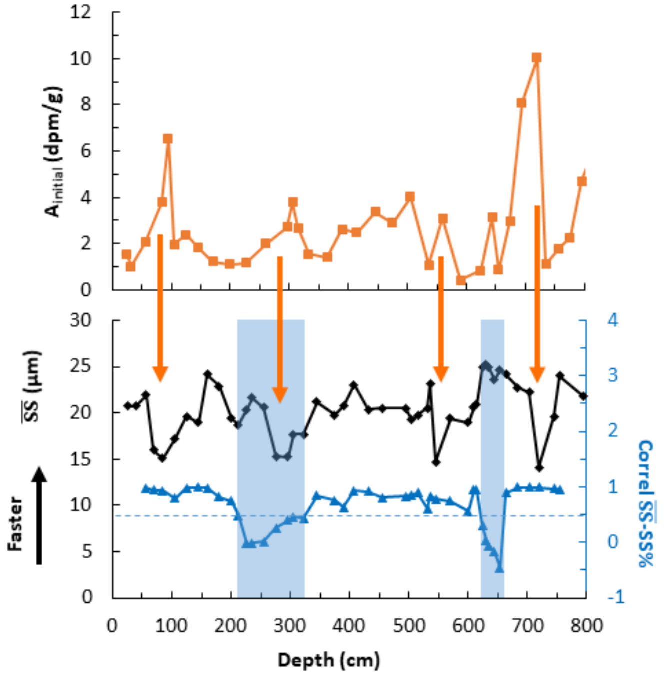

**Figure 1.8.** Comparison between initial activiy of $^{230}Th_{xs}$ ($A_{initial}$), sortable silts size -$\overline{SS}$- (µm) variation downcore and inferred paleocurrent speeds for core PS2757-8(KAL). Higher $\overline{SS}$ is indicative of faster currents. Orange arrows indicate parallels between peaks in $A_{initial}$ and dips in $\overline{SS}$, the latter indicating potentially slower current speeds. Blue line is a 5-point running correlation between $\overline{SS}$ µm and $\overline{SS}$ %; where $r < 0.5$ indicates poorly sorted silts. Dashed blue line for cut-off point $r < 0.5$, and the blue highlights mark sections below this cut off value.

### 1.5.3. Setting a stratigraphy

Broadly speaking, sedimentation rates derived from radiocarbon in the central Arctic Ocean are not uniform. Previous studies report rates of 0.2-0.3 cm/ka in the Western basin (Ku and Broecker, 1967; Clark et al., 1986). Le Duc (2018) also found low rates of ~ 0.5 cm west of the Lomonosov Ridge, which are contrasted by rates over 3 cm/ka reported in the southeastern sector of the Ridge. These differences are explained by a more dynamical sedimentary regime eastward related to sea ice transport. In addition to this geographical gradient, there is a temporal gradient: Darby et al. (1997) reports that sedimentation rates varied from less than 0.5 cm/ka during glacial regimes to 1-2 cm/ka during interglacial regimes in cores of the western Arctic Ocean. Concerning the study sites, Matthiessen et al. (2001) dated neighboring core PS2757-7 using two near surface radiocarbon dates and obtained an average sedimentation rate of ~ 7 cm/ka. Since this rate is determined from sediments that were most likely deposited during the current interglacial, it would be expected that the sedimentation rate obtained is faster than the average sedimentation rate downcore. In addition, these dates come from samples in the first 5 cm of the core, which could well be in the mixed layer that was found to be between 2 and 8 cm in cores from the Lomonosv Ridge (Le Duc, 2018).

Since radiocarbon dating of marine carbonates is only reliable up to ~ 35 ka, U-series were used for a longer timeframe. In most sequences that used the U-series to calculate sedimentation rates in the Arctic Ocean, the values range between 0.1 and 0.4 cm/ka (Ku and Broecker, 1967; Huh et al., 1997; Not and Hillaire-Marcel, 2010; Gusev et al., 2013; Hillaire-Marcel et al. 2017). Thus PS2757 seems to have an average sedimentation rate that is an order of magnitude higher than those sequences. This fact allows the observation in greater detail of the profile in $^{230}Th_{xs}$ above the depth affected by mobility.

Figures 1.9. illustrates a simple model based on steady state conditions, i.e., constant accumulation rate and initial $^{230}Th$ fluxes, fit with the calculated excesses and an age constraint discussed below. It shows:

I) $^{230}Th_{xs}$-values from measurements.
II) the theoretical decay curve of the production of $^{230}Th$ from the overlying water column (vertical $^{230}Th$ “rain”).
III) the theoretical decay curve with a $^{230}Th_{xs}$-inventory similar to that measured in the sedimentary column (effective $^{230}Th$ “rain”).

The excesses calculated from measurements fall below 2σ uncertainty on the excess at ~ 580 cm downcore, suggesting that the extinction of $^{230}Th_{xs}$ has been reached. The 2σ uncertainty on the excess is estimated with the quadratic sum of the standard deviation and analytical uncertainty on $^{238}U$ in the zone above uranium mobility. In the present case, some uncertainty prevails with respect to the depth at which $^{230}$Th$_{xs}$ may be considered "extinct", due to it being in the diagenetic U-mobility zone. Nevertheless, an age can be calculated from $t = \frac{1}{\lambda_{230}} \ln \frac{A_{initial}}{A}$, where $A_{initial}$ = 2.46 ± 0.02 dpm/g (surface activity of $^{230}$Th$_{xs}$) and A = 0.13 ± 0.01 dpm/g. This gives an extinction age of $321^{+11}_{-10}$ ka and an average sedimentation rate of 1.8 cm/ka.

The effective $^{230}$Th ‘’rain’’ decay curve was obtained using the following equation:
Cumulative $^{230}$Th$_{xs}$ (dpm/cm$^2$) =

$$\sum_{i}^{n}(t_n - t_{n-1})(\mathrm{ka}) * \text{Effective 230Th ''rain''} \left(\frac{\mathrm{dpm}}{\mathrm{cm2*ka}}\right) * e^{-\lambda * \bar{t}}$$

- Where the effective $^{230}$Th ‘’rain’’ flux is found through iterations to match the inventory of $^{230}$Th$_{xs}$ in the top 560 cm. A flux of 4.52 dpm/cm$^2$/ka was found.
- The age t (ka) is obtained with $t_n$ = Σ mass (g) * 0.4788 (ka/g).
  Since at a depth of 520.5 cm, the assigned age is 243 ka and Σ mass = 507.7g, 243 ka / 507.7 g = 0.4788 (ka/g). The age assignment was not based on the extinction depth due to the latter being in the U-mobility zone, but it was instead based on the assignment described in figure 1.11.
- $\bar{t}$ is $(t_n+t_{n-1})/2$

The vertical $^{230}$Th ‘’rain’’ decay curve was obtained in the same manner, with a flux of $^{230}$Th set to 2.63 $\frac{dpm.}{cm^2 x\ km\ x\ ka}$ (Lalou and Nguyen, 1985).

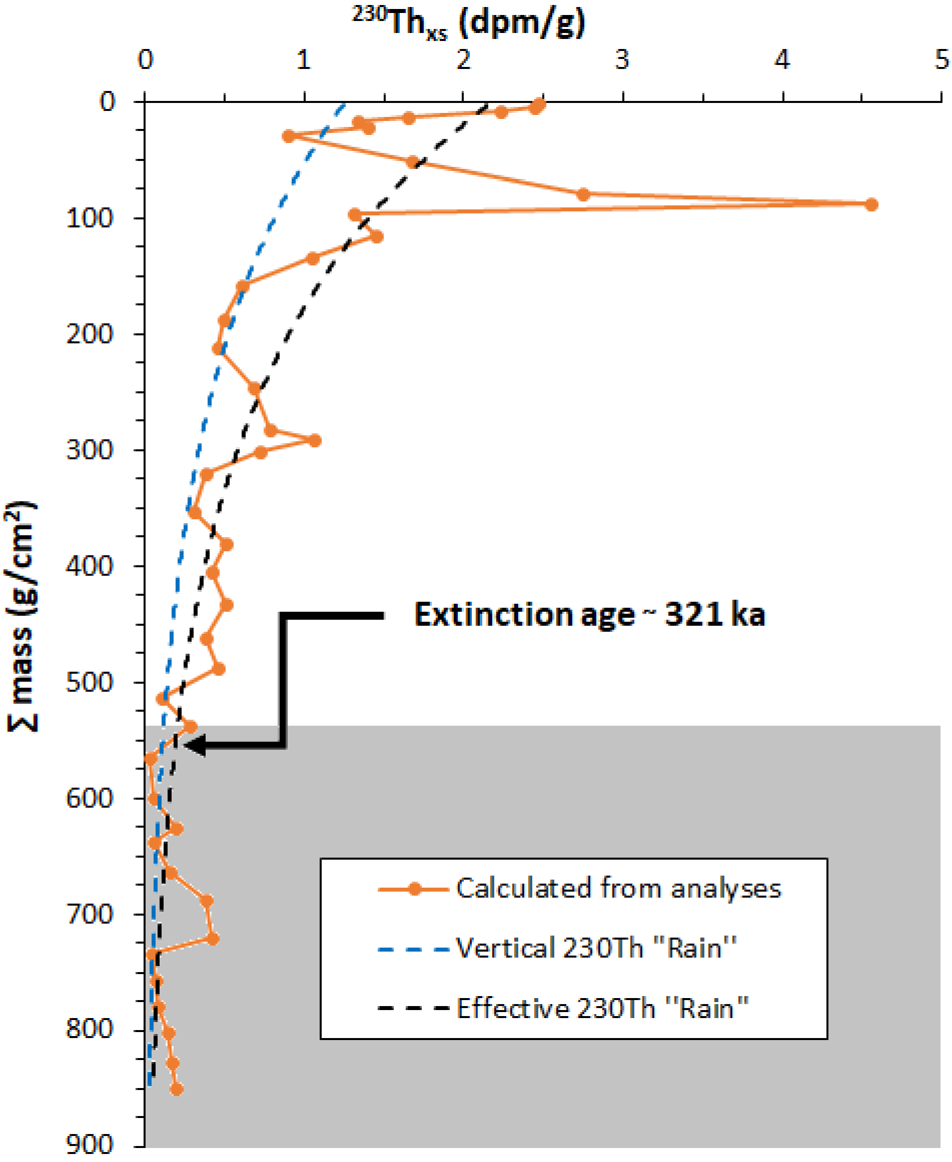

**Figure 1.9.** Measurable excess in $^{230}$Th versus $^{238}$U and decay curve under steady state conditions calculated from the $^{230}Th_{xs}$ inventory above 560 cm. Calculated extinction age of ~ 321 ka at ~ 580 cm downcore. Vertical $^{230}$Th "Rain" is the theoretical decay curve of scavenged $^{230}$Th produced in the overlying water column, assigning an age of 243 ka at 520 cm (i.e., Termination III). Grey shading indicates the zone of inferred U-mobility below ~ 560 cm.

Another possible approach to obtain age constraints is to make a range of cumulative excess curves with steady state conditions that encompasses the fluctuations in cumulative excess from measurements, and that have the same inventory of $^{230}Th_{xs}$ up to the depth of diagenetic mobility at 560 cm (Figure 1.10). The best fit curve is found in a similar manner as for figure 1.9 through iterations, while minimizing the sum of errors between the model and the measured excesses. For this curve, an age of 231 ka at 560 cm and thus sedimentation rate of 2.4 cm/ka was calculated. For the range of curves the age at 560 cm varies between 328 and 161 ka, giving sedimentation rates between 1.7 and 3.5 cm/ka. It can be seen that the measured and modelled best fit cumulative $^{230}Th_{xs}$ approaches an asymptotic value to a steady state with constant $^{230}Th_0$.

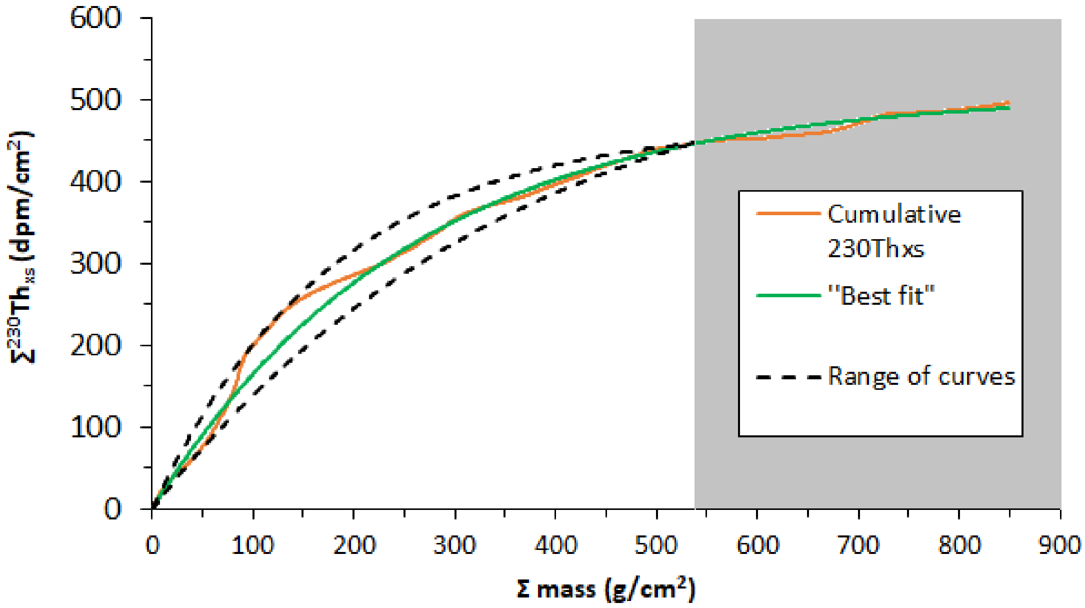

**Figure 1.10.** Observed cumulative $^{230}Th_{xs}$ inventory versus a best-fit curve calculated under steady state conditions (flux and sedimentation rate constant), and the range of curves that encompass the fluctuations in the measured $^{230}Th_{xs}$ inventory curve. Grey shading indicates the zone of inferred U-mobility below ~ 560 cm.

A more empirical approach can also be used to infer the current stratigraphy of the studied sequence. It consists in correlating the $^{230}Th_{xs}$ peaks in the sequence with those from other sites with no apparent U-mobility and very low sedimentation rates. To this effect, the study core was compared to the sequences studied by Not and Hillaire-Marcel (2010) and Hillaire-Marcel et al., (2017), both estimating extinction ages in a 300 to 375 ka range. These authors defined the $^{230}Th_{xs}$ peaks observed in their study cores to specific isotopic stages, with the $^{230}Th_{xs}$ from MIS1 to MIS 3 mixed in at core top (due to a MIS 2 sedimentary gap), and two lower peaks assigned respectively to MIS 5e and 7. Assuming a similar temporal variability in $^{230}Th$ fluxes to the sea floor at site PS2757, stratigraphy inferences can be made (Fig. 1.11). At site PS2757, sedimentation rates are significantly higher than those observed at sites investigated by Not and Hillaire-Marcel (2010) and Hillaire-Marcel et al., (2017). As a consequence, the Holocene and MIS 3 $^{230}Th_{xs}$ peaks can be clearly distinguished from each other, whereas they overlap in the very low sedimentation rate sites, in particular due to the sedimentary hiatus during MIS 2 observed quite generally in central Arctic sequences (e.g., Nørgaard-Pedersen et al., 2003).

Based on the above correlation, the MIS7/8 boundary (~ 243 ka; Lisiecki and Raymo, 2005), would be reached at ~ 520 cm down the study core (figure 1.11). The average sedimentation rate would thus be ~ 2.1 cm/ka. According to this stratigraphic scheme, the of ≥ 300 ka extinction age (≥ 4 half-lives of $^{230}Th$), as proposed by Not and Hillaire-Marcel, 2010; Hillaire-Marcel et al., 2017), at approximately or slightly below the 560 cm transition with the diagenetically altered $^{230}Th_{xs}$ profile.

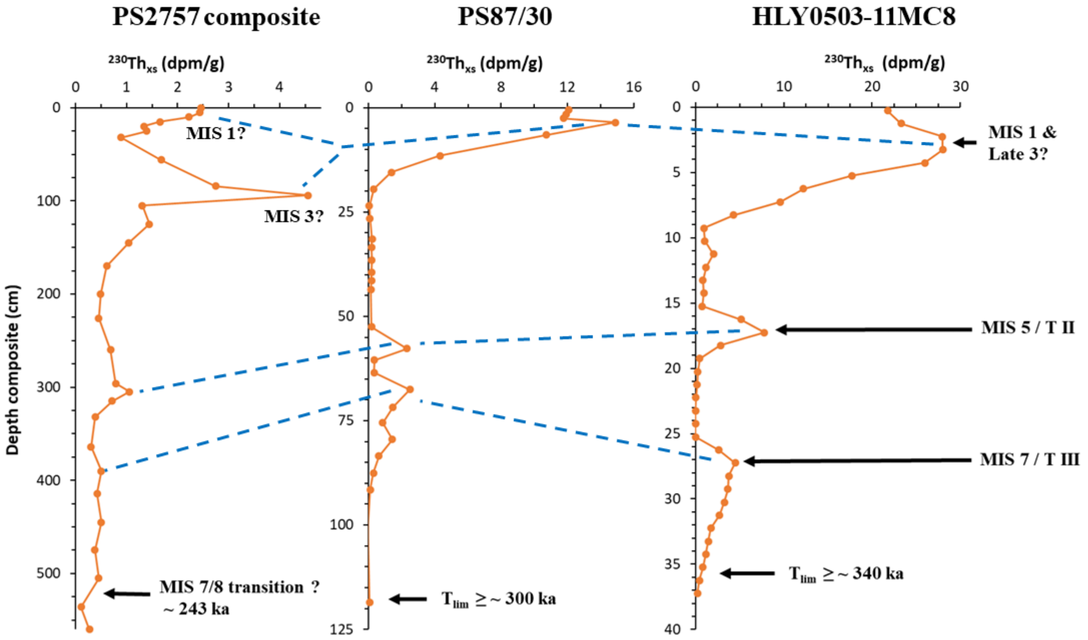

**Figure 1.11.** Correlations with core PS87/30 (Hillaire Marcel et al., 2017) and HLY0503-11MC8 (Not and Hillaire-Marcel, 2010) The four peaks observed in the composite PS2757 sequence are assigned to MIS 1, 3, 5e, and 7.

To summarise this last section, three methods to find age constraints and sedimentation rates were employed: First the age of the layer at which the excess falls below errors had a calculated age of 321 ka at 580 cm, giving a sedimentation rate of 1.8 cm/ka. Secondly, a best fit curve of cumulative excesses above 560 cm gave an age of 231 ka and a rate of 2.4 cm/ka. Lastly, the peaks in excesses were correlated with cores that had been given age constraints with $^{230}Th_{xs}$ and $^{231}Pa_{xs}$, and at 520 cm an age of 243 ka was assigned which gives a rate of 2.1 cm/ka. These three approaches considered as a whole suggest a mean sedimentation rate of 2.1 ± 0.3 cm/ka.

## 1.6. CONCLUSION

In this study, we documented the potential use of the $^{230}Th_{xs}$ chronostratigraphic approach at a site with sedimentation rates about one order of magnitude higher than those of sites where it has previously been used. Whereas the higher sedimentation rate results in a better resolution of the $^{230}Th_{xs}$ profile, allowing particularly to distinguish $^{230}Th_{xs}$ peaks matching the Holocene and MIS 3, it may result in difficulties for the setting of the effective "$^{230}Th_{xs}$ extinction age" downcore, due to the very low residual activities downcore. The difficulty is enhanced here by late diagenetic U-redistribution downcore in relation to strong redox gradients induced by the deposition of a Corg rich layer. Nevertheless, the correlation of peaks/excursions in $^{230}Th_{xs}$ with those observed elsewhere still provide a means to identify interglacials and interstadials intervals with enhanced and finer sedimentation. During such intervals, variations in paleocurrents inferred from the sortable silt fraction, seem to match $^{230}Th_{xs,}$ thus its advection to the study site.

The $^{230}Th_{xs}$ inventory was found to be significantly higher at the study site, at near proximity of the Laptev Sea slope, in comparison with sites from the central Arctic Ocean, confirming the importance of boundary scavenging of particle-reactive nuclides at the ocean basin margins. Additionally, variations in paleocurrents were inferred from the sortable silt fraction, which could potentially be linked to the variations in $^{230}Th_{xs}$.

The objective of setting a chronostratigraphy of the composite record was partly accomplished by correlating the peaks/excursions in $^{230}Th_{xs}$ with those of cores that had been accurately dated by the $^{230}Th_{xs}$ method. An average sedimentation rate of 2.1 cm/ka is retained here, based on the assignment of the fourth $^{230}Th_{xs}$ peak downcore to the MIS 7/8 transition, thus to an age of ~ 243 ka at the bottom of the peak. This age assignment is in relative agreement with a "best estimate" of the "≥ 300 ka extinction age" of $^{230}Th_{xs}$ at the site, below slightly 560 cm downcore, at the transition with the diagenetically altered sequence. It is also in agreement with a steady state model of the cumulative excess (figure 1.10.)

If the $^{230}Th_{xs}$ method were to be applied to cores similar to this one, the same problems encountered could be expected; closer to shelves, with higher fluxes of organic material during interglacials/interstadials, there is a higher probability of some U-mobility due to the development of redox gradients downcore. Nevertheless, using inventories and cumulative $^{230}Th_{xs}$ curves may help estimating the decay of $^{230}Th_{xs}$. In addition, correlation of $^{230}Th_{xs}$ profiles with those of neighboring cores, with better constrained stratigraphies, seems feasible.

Finally, all studies based on U-series isotopes converge to suggest sedimentation rates ranging from mm/ka to cm/ka from the central Arctic towards the Russian margin. However, they still are generally much lower, as much as one order of magnitude in a few cases, than those based on the so-called cyclostratigraphy (e.g., Jackobsson et al, 2001; Backman et al., 2004; Polyak et al., 2013). As it is impossible to discard the ages of around 300-375 ka that are based on the decay of excess of $^{230}Th$ in the sediments, this discrepancy would require re-examining the chronological constraints used for the setting of ages behind the cyclostratigraphy.

# APPENDIX A

# ADDITIONAL FIGURE

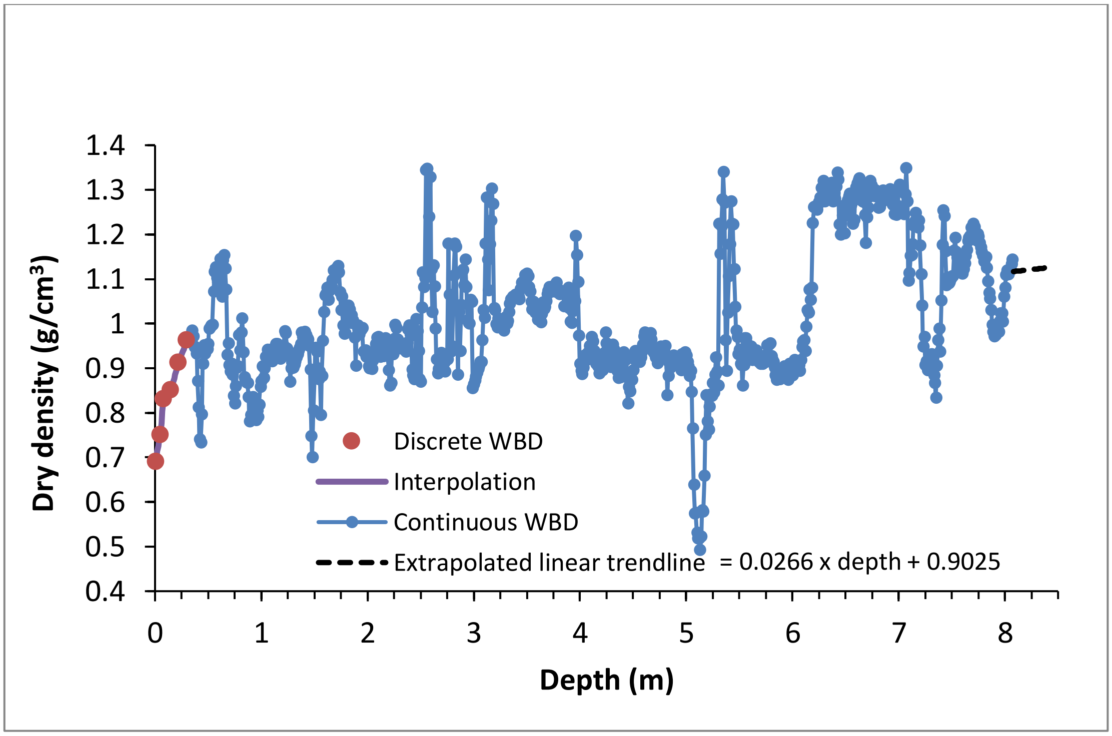

**Figure 1.12. Density profile in composite core PS2757.**

- 0-0.34 m: Discrete wet bulk density (WBD) measurements on core PS2757-7 in Rachor et al. (1997) were converted to dry bulk density (DBD) with the following equation: DBD = WBD – porosity%*$\rho_{seawater}$, where porosity is extrapolated from a linear trendline of core PS2757-8 and $\rho_{seawater}$ equals 1.025 g/cm$^3$ (Broecker & Peng,1982). Between the measured points the DBD was interpolated.
- 0.34-8.07 m: Continuous measurements of WBD on core PS2757-8 were converted to DBD with the previous equation using the measured porosity. Interpolation was used for missing depths.
- 8.07-8.38 m: DBD was extrapolated from a linear trendline of the DBD of core PS2757-8

# APPENDIX B

## TABLES OF ANALYTICAL RESULTS ON CORES PS2757-6 & PS2757-8

**Table 1.1:** U-Series isotopes analytical results (U & Th) on core PS2757-6 (MUC)

**Table 1.2**: Geochemical, isotopic and sedimentological data of core PS2757-6 (MUC)

**Table 1.3:** U-Series isotopes analytical results (U & Th) on core PS2757-8 (KAL)

**Table 1.4**: Geochemical, isotopic and sedimentological data of core PS2757-8 (KAL)

**Table 1.1:** U-Series isotopes analytical results (U & Th) on core PS2757-6 (MUC).

| **Depth (m)** | **$^{238}$U (ppb)** | **±** | **$^{232}$Th (ppb)** | **±** | **$^{234}$U/$^{238}$U (AR)** | **±** | **$^{230}$Th/$^{238}$U (AR)** | **±** | **$^{230}$Th/$^{232}$Th (AR)** | **±** | **$^{230}$Th (dpm/g)** | **±** | **$^{230}$Th$_{xs}$ vs $^{238}$U (dpm/g)** | **±** | **$^{230}$Th$_{xs}$ vs $^{234}$U (dpm/g)** | **±** |
|---|---|---|---|---|---|---|---|---|---|---|---|---|---|---|---|---|
| 0.00 | 1779 | 8 | 8757 | 68 | 0.974 | 0.006 | 2.854 | 0.020 | 1.772 | 0.017 | 3.79 | 0.02 | 2.46 | 0.02 | 2.50 | 0.02 |
| 0.05 | 2008 | 10 | 10013 | 61 | 0.965 | 0.006 | 2.629 | 0.016 | 1.611 | 0.012 | 3.94 | 0.02 | 2.44 | 0.02 | 2.49 | 0.02 |
| 0.10 | 1909 | 16 | 9723 | 54 | 0.990 | 0.011 | 2.561 | 0.024 | 1.537 | 0.011 | 3.65 | 0.02 | 2.22 | 0.02 | 2.24 | 0.02 |
| 0.15 | 1930 | 11 | 9614 | 69 | 0.984 | 0.007 | 2.147 | 0.016 | 1.317 | 0.011 | 3.09 | 0.01 | 1.65 | 0.02 | 1.67 | 0.02 |
| 0.20 | 2093 | 11 | 10454 | 92 | 0.976 | 0.007 | 1.858 | 0.012 | 1.137 | 0.011 | 2.90 | 0.01 | 1.34 | 0.02 | 1.38 | 0.02 |
| 0.25 | 2051 | 9 | 10045 | 63 | 0.991 | 0.006 | 1.729 | 0.011 | 1.079 | 0.009 | 2.65 | 0.01 | 1.12 | 0.02 | 1.13 | 0.02 |
| 0.30 | 2059 | 18 | 10176 | 74 | 1.008 | 0.010 | 1.509 | 0.015 | 0.933 | 0.008 | 2.32 | 0.01 | 0.78 | 0.02 | 0.77 | 0.01 |
| 0.34 | 2129 | 19 | 10378 | 67 | 0.995 | 0.011 | 1.448 | 0.014 | 0.908 | 0.007 | 2.30 | 0.01 | 0.71 | 0.02 | 0.72 | 0.02 |

**Table 1.2**: Geochemical, isotopic and sedimentological data of core PS2757-6 (MUC)

| **Depth (m)** | **N (%)** | **$C_{Tot}$ (%)** | **$C_{org}$ (%)** | **$\delta^{13}C$ (‰)** | **Dry bulk density ($g/cm^3$) **** |
|---|---|---|---|---|---|
| 0 | 0.12 | 1.01 | 0.83 | 22.68 | 0.69 |
| 0.05 | 0.11 | 0.68 | 0.59 | 22.68 | 0.75 |
| 0.1 | 0.09 | 0.65 | 0.67 | 22.78 | 0.84 |
| 0.15 | 0.10 | 0.53 | 0.50 | 22.96 | 0.85 |
| 0.2 | 0.11 | 0.57 | 0.51 | 23.27 | 0.89 |
| 0.25 | 0.10 | 0.53 | 0.49 | 23.30 | 0.93 |
| 0.3 | 0.10 | 0.51 | 0.49 | 23.52 | 0.96 |
| 0.34 | 0.09 | 0.46 | 0.47 | 23.48 | 0.96 |

**Dry bulk density calculated from measurements by Niessen (1996). See figure 1.12.

**Table 1.3:** U-Series isotopes analytical results (U & Th) on core PS2757-8 (KAL).

| **Depth (m)** | **$^{238}$U (ppb)** | ± | **$^{232}$Th (ppb)** | ± | **$^{234}$U/$^{238}$U (AR)** | ± | **$^{230}$Th/$^{238}$U (AR)** | ± | **$^{230}$Th/$^{232}$Th (AR)** | ± | **$^{230}$Th (dpm/g)** | ± | **$^{230}$Th$_{xs}$ vs $^{238}$U (dpm/g)** | ± | **$^{230}$Th$_{xs}$ vs $^{234}$U (dpm/g)** | ± |
|---|---|---|---|---|---|---|---|---|---|---|---|---|---|---|---|---|
| 0.25 | 2074 | 10 | 7896 | 72 | 0.980 | 0.006 | 1.902 | 0.010 | 1.527 | 0.015 | 2.94 | 0.01 | 1.40 | 0.01 | 1.43 | 0.01 |
| 0.32 | 1934 | 31 | 9885 | 75 | 1.028 | 0.020 | 1.619 | 0.028 | 0.968 | 0.010 | 2.34 | 0.02 | 0.89 | 0.03 | 0.85 | 0.02 |
| 0.56 | 2053 | 9 | 10685 | 88 | 0.971 | 0.006 | 2.096 | 0.012 | 1.231 | 0.011 | 3.21 | 0.01 | 1.68 | 0.02 | 1.72 | 0.02 |
| 0.84 | 2253 | 20 | 12431 | 97 | 0.972 | 0.011 | 2.632 | 0.026 | 1.458 | 0.013 | 4.43 | 0.02 | 2.74 | 0.03 | 2.79 | 0.02 |
| 0.94 | 2178 | 11 | 11965 | 72 | 0.991 | 0.006 | 3.800 | 0.022 | 2.114 | 0.015 | 6.18 | 0.02 | 4.55 | 0.02 | 4.57 | 0.02 |
| 1.05 | 1794 | 8 | 9674 | 63 | 1.007 | 0.006 | 1.978 | 0.011 | 1.121 | 0.008 | 2.65 | 0.01 | 1.31 | 0.01 | 1.30 | 0.01 |
| 1.25 | 1930 | 18 | 10114 | 81 | 1.006 | 0.011 | 2.006 | 0.019 | 1.170 | 0.010 | 2.89 | 0.01 | 1.45 | 0.02 | 1.44 | 0.01 |
| 1.45 | 1983 | 17 | 10783 | 98 | 0.991 | 0.010 | 1.706 | 0.015 | 0.959 | 0.009 | 2.52 | 0.01 | 1.04 | 0.01 | 1.06 | 0.01 |
| 1.70 | 1742 | 8 | 9888 | 65 | 0.979 | 0.006 | 1.471 | 0.008 | 0.792 | 0.006 | 1.91 | 0.01 | 0.61 | 0.01 | 0.64 | 0.01 |
| 2.00 | 2155 | 6 | 9771 | 68 | 0.997 | 0.004 | 1.307 | 0.006 | 0.881 | 0.007 | 2.10 | 0.01 | 0.49 | 0.01 | 0.50 | 0.01 |
| 2.26 | 1982 | 9 | 11381 | 73 | 0.945 | 0.006 | 1.309 | 0.007 | 0.697 | 0.005 | 1.94 | 0.01 | 0.46 | 0.01 | 0.54 | 0.01 |
| 2.60 | 1937 | 18 | 10676 | 95 | 1.045 | 0.012 | 1.474 | 0.015 | 0.817 | 0.008 | 2.13 | 0.01 | 0.68 | 0.02 | 0.62 | 0.01 |
| 2.96 | 2040 | 19 | 11711 | 87 | 1.012 | 0.011 | 1.517 | 0.015 | 0.807 | 0.007 | 2.31 | 0.01 | 0.79 | 0.02 | 0.77 | 0.01 |
| 3.05 | 2325 | 10 | 12345 | 82 | 0.996 | 0.006 | 1.609 | 0.008 | 0.926 | 0.007 | 2.79 | 0.01 | 1.06 | 0.01 | 1.06 | 0.01 |
| 3.15 | 2250 | 20 | 12311 | 112 | 1.001 | 0.011 | 1.426 | 0.022 | 0.797 | 0.012 | 2.39 | 0.03 | 0.72 | 0.03 | 0.71 | 0.03 |
| 3.32 | 2066 | 9 | 11312 | 94 | 1.017 | 0.006 | 1.248 | 0.007 | 0.697 | 0.006 | 1.92 | 0.01 | 0.38 | 0.01 | 0.36 | 0.01 |
| 3.64 | 2142 | 6 | 11561 | 67 | 0.980 | 0.004 | 1.191 | 0.006 | 0.674 | 0.005 | 1.90 | 0.01 | 0.30 | 0.01 | 0.34 | 0.01 |
| 3.90 | 2182 | 6 | 11437 | 101 | 0.973 | 0.004 | 1.309 | 0.007 | 0.763 | 0.008 | 2.13 | 0.01 | 0.50 | 0.01 | 0.55 | 0.01 |
| 4.14 | 1774 | 13 | 10202 | 103 | 1.020 | 0.009 | 1.320 | 0.012 | 0.701 | 0.008 | 1.75 | 0.01 | 0.42 | 0.01 | 0.40 | 0.01 |
| 4.45 | 1922 | 10 | 11525 | 89 | 0.996 | 0.010 | 1.352 | 0.008 | 0.689 | 0.006 | 1.94 | 0.01 | 0.51 | 0.01 | 0.51 | 0.01 |
| 4.75 | 1902 | 9 | 11144 | 94 | 0.993 | 0.006 | 1.266 | 0.007 | 0.660 | 0.006 | 1.80 | 0.01 | 0.38 | 0.01 | 0.39 | 0.01 |

| **Depth (m)** | **$^{238}$U (ppb)** | **±** | **$^{232}$Th (ppb)** | **±** | **$^{234}$U/$^{238}$U (AR)** | **±** | **$^{230}$Th/$^{238}$U (AR)** | **±** | **$^{230}$Th/$^{232}$Th (AR)** | **±** | **$^{230}$Th (dpm/g)** | **±** | **$^{230}$Th$_{xs}$ vs $^{238}$U (dpm/g)** | **±** | **$^{230}$Th$_{xs}$ vs $^{234}$U (dpm/g)** | **±** |
|---|---|---|---|---|---|---|---|---|---|---|---|---|---|---|---|---|
| 5.05 | 1803 | 9 | 11266 | 90 | 0.931 | 0.007 | 1.340 | 0.008 | 0.655 | 0.006 | 1.80 | 0.01 | 0.46 | 0.01 | 0.55 | 0.01 |
| 5.36 | 1521 | 8 | 8558 | 57 | 0.954 | 0.009 | 1.095 | 0.009 | 0.595 | 0.006 | 1.24 | 0.01 | 0.11 | 0.01 | 0.16 | 0.01 |
| 5.60 | 1975 | 9 | 12547 | 103 | 0.915 | 0.005 | 1.187 | 0.006 | 0.571 | 0.005 | 1.75 | 0.01 | 0.28 | 0.01 | 0.40 | 0.01 |
| 5.90 | 1763 | 18 | 10338 | 54 | 0.886 | 0.012 | 1.024 | 0.011 | 0.534 | 0.004 | 1.35 | 0.01 | 0.03 | 0.01 | 0.18 | 0.01 |
| 6.24 | 1606 | 14 | 9409 | 59 | 0.917 | 0.010 | 1.046 | 0.011 | 0.546 | 0.005 | 1.25 | 0.01 | 0.06 | 0.01 | 0.15 | 0.01 |
| 6.44 | 1401 | 12 | 8012 | 45 | 0.987 | 0.010 | 1.181 | 0.013 | 0.631 | 0.006 | 1.23 | 0.01 | 0.19 | 0.01 | 0.20 | 0.01 |
| 6.54 | 4881 | 42 | 10097 | 90 | 1.361 | 0.014 | 1.014 | 0.009 | 1.498 | 0.014 | 3.69 | 0.01 | 0.05 | 0.03 | -1.26 | 0.03 |
| 6.74 | 3758 | 32 | 10502 | 72 | 1.161 | 0.012 | 1.056 | 0.009 | 1.155 | 0.009 | 2.96 | 0.01 | 0.16 | 0.03 | -0.30 | 0.02 |
| 6.94 | 3373 | 22 | 11241 | 71 | 1.181 | 0.011 | 1.154 | 0.009 | 1.058 | 0.008 | 2.90 | 0.01 | 0.39 | 0.02 | -0.07 | 0.02 |
| 7.20 | 2207 | 9 | 8119 | 342 | 1.139 | 0.006 | 1.258 | 0.007 | 1.045 | 0.044 | 2.07 | 0.01 | 0.43 | 0.01 | 0.20 | 0.01 |
| 7.35 | 1529 | 6 | 11050 | 80 | 0.843 | 0.004 | 1.038 | 0.007 | 0.439 | 0.004 | 1.18 | 0.01 | 0.04 | 0.01 | 0.22 | 0.01 |
| 7.55 | 1587 | 10 | 10378 | 79 | 0.884 | 0.010 | 1.053 | 0.011 | 0.492 | 0.006 | 1.25 | 0.01 | 0.06 | 0.01 | 0.20 | 0.01 |
| 7.75 | 1500 | 13 | 10107 | 71 | 0.922 | 0.010 | 1.067 | 0.015 | 0.484 | 0.007 | 1.19 | 0.01 | 0.07 | 0.02 | 0.16 | 0.02 |
| 7.95 | 1635 | 6 | 11245 | 102 | 0.894 | 0.005 | 1.116 | 0.009 | 0.496 | 0.006 | 1.36 | 0.01 | 0.14 | 0.01 | 0.27 | 0.01 |
| 8.18 | 1570 | 14 | 10454 | 60 | 0.966 | 0.011 | 1.142 | 0.015 | 0.524 | 0.006 | 1.34 | 0.01 | 0.17 | 0.02 | 0.21 | 0.01 |
| 8.38 | 2142 | 18 | 10091 | 88 | 1.080 | 0.010 | 1.124 | 0.014 | 0.729 | 0.010 | 1.80 | 0.02 | 0.20 | 0.02 | 0.07 | 0.02 |

**Table 1.4**: Geochemical, isotopic and sedimentological data of core PS2757-8 (KAL)

| **Depth (m)** | **N (%)** | **C$_{Tot}$ (%)** | **C$_{org}$ (%)** | **$\delta^{13}$C (‰)** | **Sand (%)*** | **Silt (%)*** | **<2 µm, >9 phi (%)*** | **Dry bulk bulk density (g/cm$^3$)**** |
|---|---|---|---|---|---|---|---|---|
| 0.25 | 0.10 | 0.53 | 0.49 | -22.71 | 3.7 | 47.6 | 48.6 | 0.93 |
| 0.32 | 0.11 | 0.50 | 0.46 | -23.30 | 3.9 | 47.9 | 48.2 | 0.96 |
| 0.56 | 0.10 | 0.42 | 0.36 | -23.22 | 5.5 | 47.2 | 47.3 | 1.12 |
| 0.84 | 0.08 | 0.24 | 0.23 | -22.65 | 0 | 49.5 | 50.4 | 0.88 |
| 0.94 | 0.08 | 0.23 | 0.22 | -22.22 | 0 | 35 | 65 | 0.80 |
| 1.05 | 0.10 | 0.19 | 0.19 | -23.73 | 1.1 | 39 | 59.9 | 0.93 |
| 1.25 | 0.08 | 0.21 | 0.17 | -23.30 | 2.7 | 42.3 | 55 | 0.94 |
| 1.45 | 0.08 | 0.21 | 0.19 | -23.57 | 1.2 | 37.6 | 61.2 | 0.95 |
| 1.7 | 0.07 | 0.24 | 0.16 | -22.81 | 16.5 | 46.2 | 37.3 | 1.12 |
| 2 | 0.05 | 0.19 | 0.19 | -22.92 | 5 | 43 | 51 | 0.93 |
| 2.26 | 0.07 | 0.35 | 0.28 | -23.56 | 2.9 | 47.6 | 49.5 | 1.00 |
| 2.6 | | | | | 0.1 | 58.3 | 41.7 | 1.12 |
| 2.96 | 0.06 | 0.16 | 0.16 | -22.72 | 0 | 56.8 | 43.1 | 1.00 |
| 3.05 | 0.07 | 0.17 | 0.15 | -22.48 | 1.6 | 41.5 | 56.9 | 0.90 |
| 3.15 | 0.05 | 0.14 | 0.13 | -22.71 | 0.2 | 59.7 | 40.1 | 1.18 |
| 3.32 | 0.06 | 0.22 | 0.18 | -22.81 | 2.9 | 48.6 | 48.5 | 1.01 |
| 3.64 | 0.08 | 0.26 | 0.19 | -22.86 | 2.6 | 51.8 | 45.6 | 1.02 |
| 3.9 | 0.09 | 0.19 | 0.17 | -23.10 | 10.5 | 40.5 | 49 | 1.03 |
| 4.14 | 0.09 | 0.19 | 0.19 | -23.28 | 3.6 | 42.3 | 54.1 | 0.92 |
| 4.45 | 0.09 | 0.15 | 0.14 | -23.37 | 4.8 | 35.2 | 60 | 0.82 |
| 4.75 | 0.09 | 0.16 | 0.15 | -23.39 | 2.7 | 36.4 | 60.9 | 0.93 |
| 5.05 | 0.07 | 0.16 | 0.15 | -23.32 | 0.9 | 23.8 | 75.3 | 0.85 |
| 5.36 | 0.04 | 0.11 | 0.09 | -23.03 | 30.4 | 44.8 | 24.8 | 1.27 |
| 5.6 | 0.07 | 0.15 | 0.14 | -23.40 | 0.2 | 37.3 | 62.5 | 0.94 |
| 5.9 | 0.06 | 0.19 | 0.17 | -23.19 | 1.9 | 39.2 | 58.9 | 0.89 |
| 6.24 | 0.06 | 0.13 | 0.12 | -23.39 | 16.4 | 56.3 | 27.3 | 1.27 |
| 6.44 | | | | | 26.9 | 46.8 | 26.3 | 1.22 |
| 6.54 | 0.06 | 0.51 | 0.47 | -24.50 | 14.9 | 53 | 32.1 | 1.29 |
| 6.74 | 0.07 | 0.67 | 0.57 | -24.90 | 5.6 | 59.7 | 34.7 | 1.31 |
| 6.94 | 0.08 | 0.82 | 0.67 | -25.05 | 2.7 | 58.8 | 38.5 | 1.27 |
| 7.2 | 0.08 | 0.31 | 0.23 | -23.44 | 0.1 | 41.9 | 58 | 1.18 |
| 7.35 | 0.07 | 0.23 | 0.19 | -23.70 | 0 | 36.9 | 63.1 | 0.83 |

| | | | | | | | | |
|---|---|---|---|---|---|---|---|---|
| 7.55 | 0.07 | 0.27 | 0.16 | -22.86 | 7 | 52.7 | 40.4 | 1.15 |
| 7.75 | 0.07 | 0.18 | 0.18 | -23.29 | 6.7 | 57.1 | 36.2 | 1.19 |
| 7.95 | | | | | 3.4 | 47.3 | 49.3 | 1.00 |
| 8.18 | | | | | 4.6 | 49.2 | 46.1 | 1.12 |
| 8.38 | | | | | 3.4 | 59.9 | 36.7 | 1.12 |

*Granulometry from Müller and Stein (2000). **Dry bulk density calculated from measurements by Niessen (1996). See figure 1.12.

# APPENDIX C

# URANIUM AND THORIUM ISOTOPE ANALYSIS BY MC-ICP-MS FOR THE DETERMINATION OF $^{230}Th_{XS}$ IN MARINE SEDIMENTS

## Introduction

The decay series of uranium and thorium contain radioactive isotopes of several elements. The diverse geochemical properties of these elements cause some nuclides in the chain to undergo differential fractionation depending on the environment. The analysis of the isotopes in this chain therefore makes it possible to reconstruct the phenomena of transport and accumulation of these elements (Cuny-Guirriec, 2016).

This work explains the methodology of uranium and thorium isotope analysis. This method is used to create a chronostratigraphy of the central Arctic Ocean based on the $^{230}Th_{xs}$. The $^{230}Th_{xs}$ determination provides age constraints for sediment and thus estimates sedimentation rates for the central Arctic Ocean, a place where other techniques are difficult to apply (Cuny-Guirriec, 2016).

## Preparation

Sediment samples from the Central Arctic Ocean were sent to GEOTOP for analysis. The steps described below are performed to measure U-Th isotopes.

1. Dry the samples in a drying oven at 70°C for ≈ 12h.

2. Grind the samples: the samples must be ground into powder to be well digested by the acids in the subsequent steps.

3. Weigh the U-Th spike and dry it on a hot plate at 85°C for ≈ 1h.. The tracer is composed of isotopes of U and Th in an acid solution. It must be dried before weighing the samples, otherwise the acid solution reacts with the samples during weighing, which distorts the measurement. The tracer contains uranium and thorium with certified isotopic concentrations and ratios.

4. Weigh the samples. The mass of the weighed samples and tracers is approximately 0.2 g. This quantity produces concentrations that allow for proper analysis by the MC-ICP-MS once all preparatory steps have been completed.

**<u>Digestion</u>**

1. Aqua regia: a mixture of concentrated $HNO_3$ and HCL 6M is applied to the samples, then the samples are dried on a hot plate to evaporate the acids. $HNO_3$ destroys organic matter and oxidizes sulphides. It reacts with HCl to form aqua regia according to the following reaction:
   $3HCl + HNO_3 \rightarrow 2H_20 + NOCl + Cl_2$.
   Aqua regia is adequate to dissolve most sulphates, sulphides, oxides and carbonates, but only gives partial digestion (Gaudino et al., 2007).

2. HF: Then HF is carefully applied the sample, as well as concentrated $HNO_3$, and the samples are dried on a hot plate to evaporate the acids. HF can dissolve silicates according to the following reactions:

$4HF + SiO_2 \rightarrow SiF_4 (Gas) + 2H_2O.$

$6HF + SiO_2 \rightarrow H_2SiF_6 + 2H_2O.$

This acid is therefore used to dissolve the silicate matrix. Since actinides such as U and Th are not soluble in HF, $HNO_3$ is added to dissolve these elements (Connelly, 2017).

3. Boric: Once the samples are dry, a boric acid solution ($HCL + H_3BO_3$) is poured over the samples to neutralize the remaining HF and then the samples are dried on a hot plate to evaporate the acids. This step is necessary because the remaining HF from the previous step is very dangerous (an exposure of 160 $cm^2$ of skin is fatal). HF has a high vapour pressure that increases with its concentration. It therefore evaporates and its concentration is minimized during drying. However, there are still fluorine salts (e.g. NaF) in the containers after drying. These salts can then dissolve in an aqueous solution and form HF again, posing a danger (Özcan et al, 2012; Wilson et al, 2006; Connelly, 2017). Boric acid acts by complexing with fluorine, forming a tetrafluoroboric acid according to the following reactions:

   $H_3BO_3 + 3HF \rightarrow HBF_3(OH) + 2H_20$

   $HBF_3(OH) + HF \rightarrow HBF_4 + H_2O$

4. Centrifugation: Samples are dissolved in 6M HCl and then centrifuged to remove solid residues.

## Separation columns

The separation of the elements to be analysed is done by chromatographic columns. These columns contain ionic exchange resins, which are polymers containing a large number of functional groups that act as labile ions. These ions can exchange with other ions without physical changes in the structure of the resin. To ionize the resin, it must be soaked with a solution. It can then adsorb some elements or release them depending on the solution used (Ivanovich and Harmon, 1992).

### U-Th separation

For the separation of uranium and thorium, 2 ml of AG1X8 resin is used. Two acids are used: first, HCl is used to recover Th, then $HNO_3$ is used for U. The first three steps form the packaging and correctly place the resin by varying the volume of the grains that make it up (Vallière, 1997).

1. HCl 6M passes through the column to wash the resin from potential thorium contamination. Indeed, there is no adsorption of thorium in a HCl 2 solution. In the presence of HCl, uranium is complexed into $(UO_2Cl_3)^-$ and $(UO_2Cl_4)^{2-}$. It is then adsorbed onto the resin, while thorium passes through the column (Ivanovich and Harmon, 1992).

2. Then, washing with water is used to wash the uranium resin. Since the adsorption of uranium on the resin is proportional to the concentration of HCl (Ivanovich and Harmon, 1992), a water wash releases uranium from the resin.

3. HCl 6M is used again. This step releases the remaining thorium and gives the resin the right conditions to fixate the uranium during the next step.

4. A beaker is placed under the column to recover the thorium.

5. The sample dissolved in HCl 6M is poured. Uranium binds to the resin while thorium passes through.

6. HCl 6M is poured to recover the thorium. Other metals such as rare earths, alkalis, alkaline earth metals, Al, Ni, etc. pass through the columns without adsorption (Korkisch, 1988). The thorium will therefore have to be purified subsequently.
7. Beakers are placed under the columns to receive the uranium.

8. Water is poured to recover the uranium. Iron (III) follows the same path as uranium and will have to be removed later. Both elements are adsorbed in HCl solution, and their distribution coefficient is relatively proportional to the molarity of the solution. So, when washed with water these elements are released from the resin (Korkisch, 1988).

9. $HNO_3$ 7M is poured. This step continues the recovery of uranium.

10. Water is poured in. This step continues the recovery of uranium. Also, the $HNO_3$ 7M from the previous step is driven out, which reduces the degradation of the resin and allows it to be stored for reuse of the column in the next step.

### Thorium purification

For thorium purification, the AG1X8 resin is used again. Thorium is adsorbed to the resin in a solution of $HNO_3$. It forms stable nitrate complexes of the form $Th(NO_3)_6^{2-}$ (Ivanovich and Harmon, 1992), and its distribution coefficient increases with molarity, up to a maximum of 8M. In comparison, uranium has a much lower absorption in this acid. To elute Th, the best eluent is HCl 2-12M (Korkisch, 1988).

1. Washing with $HNO_3$ 7M. This step fixes the thorium if the resin is contaminated with this element. Thorium is adsorbed to the resin in a solution of $HNO_3$.

2. Wash with water. This step prevents the creation of aqua regia by mixing $HNO_3$ and HCl, which would degrade the resin.

2. Washing with HCl 6M to remove any thorium contamination.

4. Washing / conditioning with $HNO_3$ 7M. This step gives the resin the right conditions to fixate the thorium during the next step

5. Loading of the dissolved sample into 7M $HNO_3$. The thorium fixates itself on the resin.

6. Wash with $HNO_3$ 7M to allow the other elements to drain off.

7. Small Savillex™ vials are placed under the columns to receive the thorium.

8. HCl 6M is poured to recover the thorium. The samples are dried to evaporate the acids.

### Uranium purification

For uranium purification, UTEVA resin is used. About 0.250 ml is poured into columns. This resin is chosen because it retains only U, Th and actinides in $HNO_3$ solution. This removes contaminants such as Fe, Pb and Bi. The distribution coefficient is proportional with molarity; $Kd \approx 200$ to 3M, and $Kd \approx 10$ to 0.02M (Adriaens, 1992). These concentrations can therefore be used to retain and then elute uranium. As for the first column, the first 3 steps correctly place the resin by varying the volume of the grains that constitute it and wash the resin of possible uranium contamination (Vallière, 1997).

1. First, $HNO_3$ 3M is poured. Potential uranium contamination is retained.

2. Wash with water.

3. Wash with $HNO_3$ 0.02M. Potential uranium contamination is removed.

4. Wash with $HNO_3$ 3M. This step allows the resin to retain the uranium in the next step.

5. The sample dissolved in $HNO_3$ 3M is poured into the column, and the uranium is retained.

6. $HNO_3$ 3M is poured. The other contaminants are removed from the column.

7. Small Savillex™ containers are placed under the columns to receive the uranium.

8. $HNO_3$ 0.02M is poured and the uranium is recovered. The samples are dried to evaporate the acids. Once the U and Th samples are dry, they are dissolved in concentrated $HNO_3$ for their measurement on the MC-ICP-MS.

## MC-ICP-MS

### Theory

The analysis of U and Th is performed by a multicollector inductively coupled plasma mass spectrometer (MC-ICPMS) Nu Plasma II. The advent of this method has improved the sensitivity, speed, and possibly accuracy of measurements in the uranium series (Bourdon et al., 2003). The sample to be evaluated is dissolved in 2% $HNO_3$. It is then sucked into a nebulization chamber where it is dispersed as an aerosol before being sent into an argon plasma. The plasma pulls electrons from the elements to be analyzed, which transforms them into positive ions. The samples were purified in the previous steps because without these steps the ionization energy would be diluted for all sample elements and the accuracy of the analysis would be reduced.

The ions are then accelerated by an electrical potential gradient (≈6kV) and concentrated into a beam by a series of slits and electrically charged plates. The beam then passes through an energy filter. This filter consists of two curved plates that are electrically charged. The inner plate has a negative charge that attracts ions, while the outer plate has a positive charge that repels ions. Only ions with a specific range of kinetic energy can pass through this filter (Speakman, 2017).

Then the ions pass through a magnetic field that curves their trajectory in a radius proportional to their mass to charge ratio. The radius of curvature of the ions can be calculated with the following formula (Cuny-Guirriec, 2016).

$$\frac{m}{z} = r^2B^2/2V$$

where m=masse ; z=charge ; r=radius ; B=magnetic field ; V=potential.

After the magnetic field, the ions pass through a last filter, the electrostatic filter. It consists of charged plates that slow down the ions and leave only those ions with a specific mass (Speakman, 2017). Finally, the ions are counted on an ion counter and the concentration of each isotope is determined from the number of detected counts. The ion counter consists of a series of dynodes that eject secondary electrons when they are struck by an ion or electron. The cascade of electrons generated in this way provides a measurable electrical current (Hacettepe University, 2018).

**Procedure**

1. Measure the HU-1 standard by immersing the suction tube in a solution of this standard. This standard contains the natural isotopes of uranium in their natural relative abundances, with a known concentration of uranium. Once the isotopic ratios are measured, the following calculation is performed to ensure that the mass fractionation of the instrument is minimized.

   Calculation of the fractionation factor with measured $^{238}U/^{235}U$ :
   $\beta = (R_{Measured\ 238U/235U} / R_{Natural\ 238U/235U}) - 1)/\Delta M$
   Application of the fractionation factor to measured $^{235}U/^{234}U$ :
   $R_{Corrected\ 235U/234U} = R_{Measured\ 235U/234U} / (\beta x \Delta M + 1)$
   With RA/B = isotopic ratio of A to B, $\Delta M$ = mass difference between A and B, $\beta$ = fractionation factor.

   If $R_{Corrected\ 235U/234U}$ deviates by more than 1% from the natural ratio, the instrument is adjusted, and the standard analyzed again to see if the adjustment gives fairly accurate measurements.

Fractionation is caused by, among other things, the preferential transmission of heavy isotopes during their acceleration in plasma. Indeed, lighter ions migrate to the periphery of the plasma and therefore have a lower probability of being transmitted (Montaser, 1998). Other less well-known factors also cause fragmentation.

2. Washing: between each measurement the suction tube is immersed in a clean solution of 2% $HNO_3$ to prevent contamination of previous samples.

3. Measure the HU-1 + SP standard: This solution contains the HU-1 standard, as well as a U-Th tracer, and for this and subsequent samples, a different analysis from the previous one is performed for uranium. Since $^{238}U$ is much more abundant than other isotopes, this poses a problem when measuring ratios on the ion counter. Indeed, the dilution used to measure $^{238}U$ uses a concentration too low to accurately measure other isotopes. To avoid this problem, we do not measure the $^{238}U$. Instead, the $^{238}U$ content is calculated by multiplying the $^{235}U$ content by the natural ratio of these two isotopes ($^{238}U/^{235}U = 137.88$). For the measurement of thorium isotopes, another analysis is started on the instrument and then a wash is performed.

   The instrument does not measure concentrations, only isotopic ratios. However, knowing the concentrations of $^{229}Th$, $^{233}U$ and $^{236}U$ in the certified tracer, it is possible to calculate the concentrations of all isotopes from the measured isotope ratios. The values obtained by this calculation are compared with the values of the standard and the tracer, and if the results are correct, the analysis of the samples can begin.

4. The samples are analyzed: Uranium is measured in the same way as for the HU-1 and tracer standard, then a short wash is carried out. Thorium is measured in two steps to increase the accuracy of the measurements. Indeed, natural samples contain

a high content of $^{232}$Th, which is about $10^4$ to $10^5$ times higher than $^{230}$Th. Thus, to measure the $^{232}$Th/$^{229}$Th ratio, the sample is diluted so as not to exceed the capacity of the ion counter (2x$10^6$ counts/s). Thereafter, the ratio $^{229}$Th/$^{230}$Th is measured with a lower dilution. A short wash is then performed before the next sample is analyzed.

It should be noted that the mass fractionation is corrected with the following formula:

$$R_{\text{Corrected}} = R_{\text{Measured}} \text{ x } (M_A/M_B)^{\beta}$$

with R = isotopic ratio of A on B, M = molecular weight, β = fractionation factor.

$$\beta = (\ln(R_{\text{Certified 236U/233U}} / R_{\text{Measured 236U/233U}}))/(\ln(M_{236U}/M_{233U}))$$

End of session: A longer wash is performed to remove thorium that
tends to stick to the walls of the instrument. The control parameters are saved, then the plasma is cut off and lastly the plasma cooling system is cut off as well.

The measurements obtained can then be used to study the imbalances in the uranium series, particularly for dating corals, speleothems, or to provide time constraints in marine sediments (Bourdon et al., 2003).

# REFERENCES

Adriaens, A. G., Fassett, J. D., Kelly, W. R., Simons, D. S., & Adams, F. C. (1992). Determination of uranium and thorium concentrations in soils: a comparison of isotope dilution-secondary ion mass spectrometry and isotope dilution-thermal ionization mass spectrometry. *Analytical Chemistry*, *64*(23), 2945-2950.

Alkama, R., Kageyama, M., Ramstein, G., Marti, O., Ribstein, P., & Swingedouw, D. (2008). Impact of a realistic river routing in coupled ocean–atmosphere simulations of the Last Glacial Maximum climate. *Climate Dynamics*, *30*(7-8), 855-869.

Allard, G., Roy, M., Ghaleb, B., Richard, P.J.H., Larouche, A.C., Veillette, J.J., Parent, M., 2012. Constraining the age of the last interglacial-glacial transition in the Hudson Bay lowlands (Canada) using U-Th dating of buried wood. *Quaternary Geochronology*, 7 (1), 37-47.

Anderson, R. F., Lao, Y., Broecker, W. S., Trumbore, S. E., Hofmann, H. J., & Wolfli, W. (1990). Boundary scavenging in the Pacific Ocean: a comparison of 10Be and 231Pa. *Earth and Planetary Science Letters*, *96*(3-4), 287-304.

Are, F., & Reimnitz, E. (2000). An overview of the Lena River Delta setting: geology, tectonics, geomorphology, and hydrology. *Journal of Coastal Research*, 16(4), 1083-1093.

Baskaran, M. (2001). Scavenging of thorium isotopes in the Arctic regions: Implications for the fate of particle-reactive pollutants. *Marine Pollution Bulletin*, *42*(1), 16-22.

Bonatti, E., Fisher, D. E., Joensuu, O., & Rydell, H. S. (1971). Post depositional mobility of some transition elements, phosphorus, uranium and thorium in deep sea sediments. *Geochimica et Cosmochimica Acta*, *35*(2), 189-201.

Bourdon, B., Turner, S., Henderson, G.M., Lundstrom, C.C. (2003). Introduction to U-series Geochemistry. *Reviews in Mineralogy and Geochemistry*, 52 (1), 1–21. https://doi.org/10.2113/0520001

Broecker, W. S. & Peng, T. H. (1982). *Tracers in the Sea*. Eldigio Press, Palisades.Chabaux, F., Bourdon, B. and Riotte, J. (2008). U-Series Geochemistry in Weathering Profiles, River Waters and Lakes. *Radioactivity in the Environment*, 13, 49-104.

Chen, J. H., Edwards, R. L., & Wasserburg, G. J. (1986). 238U, 234U and 232Th in seawater. *Earth and Planetary Science Letters*, 80(3-4), 241-251.

Cheng, H., Edwards, R. L., Hoff, J., Gallup, C. D., Richards, D. A., & Asmerom, Y. (2000). The half-lives of uranium-234 and thorium-230. *Chemical Geology*, 169(1–2), 17–33.

Clark, D. L., Whitman, R. R., Morgan, K. A., & Mackey, S. D. (1980). Stratigraphy and glacial-marine sediments of the Amerasian Basin, central Arctic Ocean. *Special Paper of the Geological Society of America*, 181, 1-57.

Clark, D. L., & Hanson, A. (1983). Central Arctic Ocean sediment texture: a key to ice transport mechanisms, in: Molnia, B. F. (Ed), *Glacial-marine sedimentation*. (pp. 301-330). Springer, Boston.

Clark, D. L., Andree, M., Broecker, W. S., Mix, A. C., Bonani, G., Hofmann, H. J., ... & Woelfli, W. (1986). Arctic Ocean chronology confirmed by accelerator 14C dating. *Geophysical Research Letters*, *13*(4), 319-321.

Colley, S., Thomson, J., Wilson, T. R. S., & Higgs, N. C. (1984). Post-depositional migration of elements during diagenesis in brown clay and turbidite sequences in the North East Atlantic. *Geochimica et Cosmochimica Acta*, *48*(6), 1223-1235.

Colley, S., Thomson, J., & Toole, J. (1989). Uranium relocations and derivation of quasi-isochrons for a turbidite/pelagic sequence in the Northeast Atlantic. Geochimica et Cosmochimica Acta, 53(6), 1223-1234.

Connelly, A. (2017, March 26). *The use of hydrofluoric acid in the laboratory*. Andy Connely. https://andyjconnelly.wordpress.com/2017/03/26/the-use-of-hydrofluoric-acid-in-the-laboratory/potentials and limits.

Coplen, T. B., Brand, W. A., Gehre, M., Gröning, M., Meijer, H. A., Toman, B., & Verkouteren, R. M. (2006). New guidelines for δ 13C measurements. *Analytical Chemistry*, *78*(7), 2439-2441.

Cuny-Guirriec, K. (2016). *Chronostratigraphie sur la ride de Lomonosov (Océan Arctique) à partir des analyses de la chaine de désintégration radioactive de l’ $^{238}$U : reconstitution des flux sédimentaires sur le Quaternaire récent*. [Unpublished master thesis]. Université Paris-Saclay

DePaolo, D. J., Maher, K., Christensen, J. N., & McManus, J. (2006). Sediment transport time measured with U-series isotopes: results from ODP North Atlantic drift site 984. *Earth and Planetary Science Letters*, *248*(1), 394-410.

Deschamps, C. E., St-Onge, G., Montero-Serrano, J. C., & Polyak, L. (2018). Chronostratigraphy and spatial distribution of magnetic sediments in the Chukchi and Beaufort seas since the last deglaciation. *Boreas*, *47*(2), 544-564.

Dipre, G. R., Polyak, L., Kuznetsov, A. B., Oti, E. A., Ortiz, J. D., Brachfeld, S. A., ... & Cook, A. E. (2018). Plio-Pleistocene sedimentary record from the Northwind Ridge: new insights into paleoclimatic evolution of the western Arctic Ocean for the last 5 Ma. *arktos*, *4*(1), 24.

Doell, R. R., & Dalrymple, G. B. (1966). Geomagnetic polarity epochs: A new polarity event and the age of the Brunhes-Matuyama boundary. *Science*, 152(3725), 1060-1061.

Edmonds, H. N., Moran, S. B., Hoff, J. A., Smith, J. N., & Edwards, R. L. (1998). Protactinium-231 and thorium-230 abundances and high scavenging rates in the western Arctic Ocean. *Science*, 280(5362), 405-407.

Edwards, R.L., Chen, J.H., Wasserburg, G.J., 1987. 238U 234U 230Th 232Th systematics and the precise measurement of time over the past 500,000 years. *Earth and Planetary Science Letters*, 81, 175-192.

Eicken, H., Reimnitz, E., Alexandrov, V., Martin, T., Kassens, H., & Viehoff, T. (1997). Sea-ice processes in the Laptev Sea and their importance for sediment export. *Continental Shelf Research*, *17*(2), 205-233. https://doi.org/10.1016/S0278-4343(96)00024-6

Eicken, H., Kolatschek, J., Freitag, J., Lindemann, F., Kassens, H., & Dmitrenko, I. (2000). A key source area and constraints on entrainment for basin-scale sediment transport by Arctic sea ice. *Geophysical Research Letters*, *27*(13), 1919-1922. https://doi.org/10.1029/1999GL011132

Fahl, K., & Nöthig, E. M. (2007). Lithogenic and biogenic particle fluxes on the Lomonosov Ridge (central Arctic Ocean) and their relevance for sediment accumulation: Vertical vs. lateral transport. *Deep Sea Research Part I: Oceanographic Research Papers*, 54(8), 1256-1272.

Francois, R., M. Frank, M. M. Rutgers van der Loeff, and M. P. Bacon (2004). 230Th normalization: An essential tool for interpreting sedimentary fluxes during the late Quaternary. *Paleoceanography*, 19(1), 1018. Doi:10.1029/2003PA000939.

Gaudino, S., Galas, C., Belli, M., Barbizzi, S., de Zorzi, P., Jaćimović, R., … & Sansone, U. (2007). The role of different soil sample digestion methods on trace elements analysis: a comparison of ICP-MS and INAA measurement results. *Accreditation and quality assurance*, *12*(2), 84-93.

Grantz, A., Pease, V. L., Willard, D. A., Phillips, R. L., & Clark, D. L. (2001). Bedrock cores from 89° North: Implications for the geologic framework and Neogene paleoceanography of Lomonosov Ridge and a tie to the Barents shelf. *Geological Society of America Bulletin*, 113(10), 1272-1281.

Hacettepe University (2012, January 28). *ICP-MS Belgeler*. Hacettepe Üniversitesi ICP-MS Laboratuvari. http://www.icp.hacettepe.edu.tr/belgeler.shtml

Hélie, Jean-François (2009). Elemental and stable isotopic approaches for studying the organic and inorganic carbon components in natural samples. In *IOP Conference Series: Earth and Environmental Science*, 5(1), 012005.

Henderson, G. M., Heinze, C., Anderson, R. F., & Winguth, A. M. (1999). Global distribution of the 230Th flux to ocean sediments constrained by GCM modelling. *Deep Sea Research Part I: Oceanographic Research Papers*, *46*(11), 1861-1893

Henderson, G. M. (2002). Seawater (234U/238U) during the last 800 thousand years. *Earth and Planetary Science Letters*, *199*(1-2), 97-110.

Hillaire-Marcel, C., Aksu, A., Causse, C., Vernal, A. D., & Ghaleb, B. (1990). Response of Th/U in deep Labrador Sea sediments (ODP Site 646 to changes in sedimentation rates and paleoproductivities. *Geology*, 18(2), 162-165.

Hillaire-Marcel, C., Ghaleb, B., de Vernal, A., Maccali, J., Cuny, K., Jacobel, A., ... & McManus, J. (2017). A new chronology of late quaternary sequences from the central Arctic Ocean based on “extinction ages” of their excesses in 231Pa and 230Th. *Geochemistry, Geophysics, Geosystems*, 18(12), 4573-4585.

Hoffmann, S. S., McManus, J. F., Curry, W. B., & Brown-Leger, L. S. (2013). Persistent export of 231 Pa from the deep central Arctic Ocean over the past 35,000 years. *Nature*, 497(7451), 603.

Holmes, R. M., McClelland, J. W., Peterson, B. J., Shiklomanov, I. A., Shiklomanov, A. I., Zhulidov, A. V., ... & Bobrovitskaya, N. N. (2002). A circumpolar perspective on fluvial sediment flux to the Arctic Ocean. *Global biogeochemical cycles*, 16(4), 45-1.

Huh, C. A., Pisias, N. G., Kelley, J. M., Maiti, T. C., & Grantz, A. (1997). Natural radionuclides and plutonium in sediments from the western Arctic Ocean: Sedimentation rates and pathways of radionuclides. *Deep Sea Research*, *Part II*, 44(8), 1725–1743.

Ivanovich, M., and Harmon, R. S. (1992). Uranium-series Disequilibrium; Applications to Earth, Marine, and Environmental Sciences, second edition. Clarendon Press, Oxford.

Kigoshi, K. (1971). Alpha-recoil thorium-234: dissolution into water and the uranium-234/uranium-238 disequilibrium in nature. *Science*, 173(3991), 47-48.

Klinkhammer, G. P., & Palmer, M. R. (1991). Uranium in the oceans: where it goes and why. *Geochimica et Cosmochimica Acta*, *55*(7), 1799-1806.

Korkisch, J. (1988). CRC handbook of ion exchange resins (Vol. VI). CRC Press, Boca Raton.

Ku, T. L., & Broecker, W. S. (1965). Rates of sedimentation in the Arctic Ocean. *Progress in oceanography*, *4*, 95-104.

Lalou, C., & Nguyen, H. V. (1985). Les méthodes de datation par les déséquilibres dans les familles de l’uranium. *Méthodes de datation par les phénomènes nucléaires naturels, applications* (pp. 175-201). Masson, Paris

Lao, Y., Anderson, R. F., Broecker, W. S., Hofmann, H. J., & Wolfli, W. (1993). Particulate fluxes of 230Th, 231Pa, and 10Be in the northeastern Pacific Ocean. *Geochimica et Cosmochimica Acta*, *57*(1), 205-217.

Le Duc, C. (2018). *Flux sédimentaires le long de la ride de Lomonosov, océan Arctique*. [Master thesis, Université du Québec à Montréal]. https://www.geotop.ca/en/recherche/publications/theses_memoires

Lisiecki, L. E., & Raymo, M. E. (2005). A Pliocene-Pleistocene stack of 57 globally distributed benthic δ18O records. *Paleoceanography*, *20*(1).

Lovley, D. R., Roden, E. E., Phillips, E. J. P., & Woodward, J. C. (1993). Enzymatic iron and uranium reduction by sulfate-reducing bacteria. *Marine Geology*, 113(1-2), 41-53.

Ludwig, K. R. (2003). Mathematical–statistical treatment of data and errors for 230Th/U geochronology. *Reviews in Mineralogy and Geochemistry*, *52*(1), 631-656.

Maccali, J., Hillaire-Marcel, C., Carignan, J., & Reisberg, L. C. (2013). Geochemical signatures of sediments documenting Arctic sea-ice and water mass export through Fram Strait since the Last Glacial Maximum. *Quaternary Science Reviews*, 64, 136-151.

Maccali, J., Hillaire-Marcel, C., Ghaleb, B., Ménabréaz, L, Blénet, A., Edinger, E., Helie, J. F., & Preda, M. (2019). *Late Quaternary sporadic development of Desmophyllum dianthus deep-coral populations in the southern Labrador Sea with specific attention to their 14C and 230Th-dating* [Manuscript submitted for publication]. Geotop, Université du Québec à Montréal.

Matthiessen, J., Knies, J., Nowaczyk, N. R., & Stein, R. (2001). Late Quaternary dinoflagellate cyst stratigraphy at the Eurasian continental margin, Arctic Ocean: indications for Atlantic water inflow in the past 150,000 years. *Global and Planetary Change*, 31(1), 65-86.

McCave, I. N., Thornalley, D. J. R., & Hall, I. R. (2017). Relation of sortable silt grain-size to deep-sea current speeds: Calibration of the 'Mud Current Meter'. *Deep Sea Research Part I: Oceanographic Research Papers*, 127, 1-12.

McCave, I. N., & Andrews, J. T. (2019). Distinguishing current effects in sediments delivered to the ocean by ice. I. Principles, methods and examples. *Quaternary Science Reviews*, 212, 92-107.

McPhee, M. G., Proshutinsky, A., Morison, J. H., Steele, M., & Alkire, M. B. (2009). Rapid change in freshwater content of the Arctic Ocean. *Geophysical Research Letters*, 36(10).

Michels, J., Dieckmann, G. S., Thomas, D. N., Schnack-Schiel, S. B., Krell, A., Assmy, P., ... & Cisewski, B. (2008). Short-term biogenic particle flux under late spring sea ice in the western Weddell Sea. *Deep Sea Research Part II: Topical Studies in Oceanography*, 55(8-9), 1024-1039.

Montaser, A. (Ed.). (1998). *Inductively coupled plasma mass spectrometry*. John Wiley & Sons, Hoboken.

Moran, S. B., Charette, M. A., Hoff, J. A., Edwards, R. L., & Landing, W. M. (1997). Distribution of 230Th in the Labrador Sea and its relation to ventilation. *Earth and Planetary Science Letters*, *150*(1-2), 151-160.

Moran, S. B., Shen, C. C., Edwards, R. L., Edmonds, H. N., Scholten, J. C., Smith, J. N., & Ku, T. L. (2005). 231Pa and 230Th in surface sediments of the Arctic Ocean: Implications for 231Pa/230Th fractionation, boundary scavenging, and advective export. *Earth and Planetary Science Letters*, 234(1-2), 235-248.

Moran, K., Backman, J., Brinkhuis, H., Clemens, S. C., Cronin, T., Dickens, G. R., ... & Kaminski, M. (2006). The cenozoic palaeoenvironment of the arctic ocean. *Nature*, 441(7093), 601-605.

Morison, J., Kwok, R., Peralta-Ferriz, C., Alkire, M., Rigor, I., Andersen, R., & Steele, M. (2012). Changing arctic ocean freshwater pathways. *Nature*, *481*(7379), 66-70.

Müller, Claudia; Stein, Ruediger (2000): Sedimentology of core PS2757-8. [Data set]. PANGAEA, https://doi.org/10.1594/PANGAEA.57243

Müller, Claudia (2004): Age determinations by radiocarbon dating on sediment core PS2757-7. [Data set]. PANGEA, https://doi:10.1594/PANGAEA.143810

Naidu, A. S., Cooper, L. W., Finney, B. P., Macdonald, R. W., Alexander, C., & Semiletov, I. P. (2000). Organic carbon isotope ratios (δ 13 C) of Arctic Amerasian continental shelf sediments. *International Journal of Earth Sciences*, 89(3), 522-532.

Niessen, Frank (1996): Physical properties of sediment core PS2757-8. [Data set]. PANGAEA, https://doi.org/10.1594/PANGAEA.50569

Nørgaard-Pedersen, N., Spielhagen, R. F., Erlenkeuser, H., Grootes, P. M., Heinemeier, J., & Knies, J. (2003). Arctic Ocean during the Last Glacial Maximum: Atlantic and polar domains of surface water mass distribution and ice cover. *Paleoceanography*, *18*(3).

Not, C. (2010). *Les actinides dans les sédiments quaternaires de l'océan Arctique* [Doctoral dissertation, Université du Québec à Montréal]. https://www.geotop.ca/en/recherche/publications/theses_memoires

Not, C., & Hillaire-Marcel, C. (2010). Time constraints from 230 Th and 231 Pa data in late Quaternary, low sedimentation rate sequences from the Arctic Ocean: an example from the northern Mendeleev Ridge. *Quaternary Science Reviews*, 29(25), 3665-3675.

Not, C., Brown, K., Ghaleb, B., & Hillaire-Marcel, C. (2012). Conservative behavior of uranium vs. salinity in Arctic sea ice and brine. *Marine Chemistry*, 130, 33-39.

O'Regan, M., King, J., Backman, J., Jakobsson, M., Pälike, H., Moran, K., ... & Jordan, R. W. (2008). Constraints on the Pleistocene chronology of sediments from the Lomonosov Ridge. *Paleoceanography*, *23*(1).

O'Regan, M., Sellen, E., & Jakobsson, M. (2014). Middle to late Quaternary grain size variations and sea-ice rafting on the Lomonosov Ridge. *Polar Research*, 33(1), 23672.

Özcan, M; Allahbeickaraghi, & A; Dündar, M. (2012). Possible hazardous effects of hydrofluoric acid and recommendations for treatment approach: a review. *Clinical oral investigations*, 16(1), 15-23. http://doi.org/10.5167/uzh-62951

Pinet, P. R. (2011). Invitation to oceanography. Jones & Bartlett Publishers, Burlington.

Polyak, L., Alley, R. B., Andrews, J. T., Brigham-Grette, J., Cronin, T. M., Darby, D. A., ... & Jennings, A. E. (2010). History of sea ice in the Arctic. *Quaternary Science Reviews*, 29(15-16), 1757-1778.

Polyak, L., Best, K. M., Crawford, K. A., Council, E. A., & St-Onge, G. (2013). Quaternary history of sea ice in the western Arctic Ocean based on foraminifera. *Quaternary Science Reviews*, 79, 145-156.

Polyak, L., and M. Jakobsson. 2011. Quaternary sedimentation in the Arctic Ocean: Recent advances and further challenges. *Oceanography*, 24(3), 52–64,

Polyak, L., Bischof, J., Ortiz, J. D., Darby, D. A., Channell, J. E., Xuan, C., ... & Adler, R. E. (2009). Late Quaternary stratigraphy and sedimentation patterns in the western Arctic Ocean. *Global and Planetary Change*, 68(1-2), 5-17.

Proshutinsky, A. Y., & Johnson, M. A. (1997). Two circulation regimes of the wind-driven Arctic Ocean. *Journal of Geophysical Research: Oceans*, 102(C6), 12493-12514.

Rachor, E. (1997). Scientific cruise report of the Arctic Expedition ARK-XI/1 of RV" Polarstern" in 1995:(German-Russian Project LADI: Laptev Sea-Arctic Deep Basin Interrelations), Wissenschaftlicher Fahrtbericht über die Arktis-Expedition ARK-XI/1 von 1995 mit FS" Polarstern". *Berichte zur Polarforschung* = Reports on Polar Research, 1-226.

Reimnitz, E., Dethleff, D., & Nürnberg, D. (1994). Contrasts in Arctic shelf sea-ice regimes and some implications: Beaufort Sea versus Laptev Sea. *Marine Geology*, 119(3–4), 215–225.

Rosholt, J. N., Emiliani, C., Geiss, J., Koczy, F. F., & Wangersky, P. J. (1961). Absolute dating of deep-sea cores by the Pa231/Th230 method. *The Journal of Geology*, 69(2), 162-185.

Roy-Barman, M., Lemaitre, C., Ayrault, S., Jeandel, C., Souhaut, M., Miquel, J.C., (2009). The influence of particle composition on Thorium scavenging in the Mediterranean Sea. *Earth and Planetary Science Letters*, 286(3-4), 526-534.

Shackleton, N. J. (2000). The 100,000-year ice-age cycle identified and found to lag temperature, carbon dioxide, and orbital eccentricity. *Science*, 289(5486), 1897-1902

Schirrmeister, L., Oezen, D., & Geyh, M. A. (2002). 230 Th/U dating of frozen peat, Bol'shoy Lyakhovsky Island (northern Siberia). *Quaternary research*, 57(2), 253-258.

Schoster, Frank (2005): Geochemistry of sediment core PS2757-8. [Data set]. PANGAEA, https://doi.org/10.1594/PANGAEA.227863

Schubert, C. J., & Calvert, S. E. (2001). Nitrogen and carbon isotopic composition of marine and terrestrial organic matter in Arctic Ocean sediments: implications for nutrient utilization and organic matter composition. *Deep Sea Research Part I: Oceanographic Research Papers*, *48*(3), 789-810

Semiletov, I. P., Pipko, I. I., Shakhova, N. E., Dudarev, O. V., Pugach, S. P., Charkin, A. N., ... & Gustafsson, Ö. (2011). Carbon transport by the Lena River from its headwaters to the Arctic Ocean, with emphasis on fluvial input of terrestrial particulate organic carbon vs. carbon transport by coastal erosion. *Biogeosciences*, *8*(9), 2407-2426.

Spell, T. L., & McDougall, I. (1992). Revisions to the age of the Brunhes-Matuyama boundary and the Pleistocene geomagnetic polarity timescale. *Geophysical research letters*, 19(12), 1181-1184.

Stein, R. (2008). *Arctic Ocean sediments: processes, proxies, and paleoenvironment* (Vol. 2). Elsevier, Amsterdam.

Stein, R. (2015). The expedition PS87 of the Research Vessel Polarstern to the Arctic Ocean in 2014, Berichte zur Polar- und Meeresforschung = *Reports on Polar and Marine Research*, 688, 1–273.

Stein, R., Fahl, K., Gierz, P., Niessen, F., & Lohmann, G. (2017). Arctic Ocean sea ice cover during the penultimate glacial and the last interglacial. *Nature communications*, 8(1), 373.

Stein, R., Grobe, H., & Wahsner, M. (1994). Organic carbon, carbonate, and clay mineral distributions in eastern central Arctic Ocean surface sediments. *Marine Geology*, 119(3-4), 269-285.

Stein, R., Schubert, C., Vogt, C., & Fütterer, D. (1994). Stable isotope stratigraphy, sedimentation rates, and salinity changes in the Latest Pleistocene to Holocene eastern central Arctic Ocean. *Marine Geology*, 119(3-4), 333-355.

Strobl, C. (1998). *Datierung von Sedimentkernen und Rekonstruktion der Transportwege der Radionuklide 10Be, 230Th und 231 Pa in hohen nördlichen Breiten*. [Doctoral dissertation, Heidelberg University]. https://epic.awi.de/id/eprint/41838/

Herman Y. (Ed.). (1989). *The Arctic seas climatology, oceanography, geology, and biology*. Springer, New York.

Thomas, D. N., Papadimitriou, S., & Michel, C. (2010). Biogeochemistry of sea ice, in: Thomas, D. N., & Dieckmann, G. S. (Eds.), *Sea ice* (2nd edition). Wiley- (pp. 267–302). Blackwell, Hoboken.

Thomson, J., Higgs, N. C., & Colley, S. (1996). Diagenetic redistributions of redox sensitive elements in northeast Atlantic glacial/interglacial transition sediments. *Earth and Planetary Science Letters*, *139*(3-4), 365-377.

Thomson, J., Jarvis, I., Green, D. R., Green, D. A., & Clayton, T. (1998). Mobility and immobility of redox-sensitive elements in deep-sea turbidites during shallow burial. *Geochimica et Cosmochimica Acta*, 62(4), 643-656.

Thorez, J. (2003). L'argile, mineral pluriel. *Bulletin de la Societe Royale des Sciences de Liege*, 72(1), 19–70.

Trimble, S. M., Baskaran, M., & Porcelli, D. (2004). Scavenging of thorium isotopes in the Canada Basin of the Arctic Ocean. *Earth and Planetary Science Letters*, *222*(3-4), 915-932.

Speakman, R. J. (2017, June 2). *Overview of ICP-MS*. Archaeometry Laboratory, University of Missouri Research Reactor. http://archaeometry.missouri.edu/icpms_overview.html

Vallières, S. (1997). *Flux d'uranium et excès de 230Th dans les sédiments de la mer du Labrador – Relations avec les conditions paléocéanographiques et la paléoproductivité du bassin*. [Unpublished doctoral dissertation]. Université du Québec à Chicoutimi.

Veiga-Pires, C. C. (1998). *Flux de thorium-230 et flux sédimentaires dans l'Atlantique du Nord Ouest au cours des derniers 40 ka en relation avec les variations du climat*, [Unpublished doctoral dissertation]. Université du Québec à Montréal.

Vervoort, J., & Mueller, P. (2018, September 25). *Multicollector-Inductively Coupled Plasma Mass Spectrometer (MC-ICPMS).* Geochemical Instrumentation and Analysis.https://serc.carleton.edu/research_education/geochemsheets/techniques/MCICPMS.html

Woods Hole Oceanographic Institution. (2019, December 12). *Arctic Ocean Oscillation Index*. https://www.whoi.edu/page.do?pid=66578

Wilson, M.A., Burt, R., and Lee, C.W. (2006). Improved Elemental Recoveries in Soils with Heating Boric Acid Following Microwave Total Digestion. *Communications in Soil Science and Plant Analysis*, 37, 513–524.

Wu, G., & Hillaire-Marcel, C. (1994). Accelerator mass spectrometry radiocarbon stratigraphies in deep Labrador Sea cores: paleoceanographic implications. *Canadian Journal of Earth Sciences*, 31(1), 38-47.

Yamada, M., & Tsunogai, S. (1984). Postdepositional enrichment of uranium in sediment from the Bering Sea. *Marine geology*, 54(3-4), 263-276.

Yokoyama, T., Makishima, A., & Nakamura, E. (1999). Separation of thorium and uranium from silicate rock samples using two commercial extraction chromatographic resins. *Analytical chemistry*, 71(1), 135-141.

Yusoff, A. H., Sabuti, A. A., & Mohamed, C. A. R. (2015). Natural uranium and thorium isotopes in sediment cores off Malaysian ports. *Ocean Science Journal*, 50(2), 403-412.